INTERNATIONAL JOURNAL FOR NUMERICAL METHODS IN FLUIDS, VOL. 22, 771–798 (1996)

ON VISCOUS FLOW IN CURVED PIPES OF NON-UNIFORM CROSS-SECTION

A. M. ROBERTSON

Department of Mechanical Engineering, University of Pittsburgh, Pittsburgh, PA 15261, USA

SUMMARY

This paper is concerned with steady, laminar flow of an incompressible Newtonian fluid in curved pipes of non-uniform cross-section. During the past decade a number of numerical solutions for flow in curved pipes have been obtained using progressively improved computational methods and technology; see e.g. Soh and Berger (*Int. j. numer. methods fluids*, **7**, 733–755 (1987)) and Green *et al.* (*Phil. Trans. R. Soc. Lond. A*, **342**, 543–572 (1993)) for relevant references. These results have been confined mainly to fully developed flow in pipes of constant cross-section. The present study deals with curved pipes of variable cross-section in which the velocity field is necessarily a function of the axial location along the pipe centreline in addition to the two cross-sectional co-ordinates. We use the finite difference method on a staggered grid with Newton's method to solve the Navier–Stokes equations. Results are calculated and presented for non-uniform pipe geometries with curvature ratios of 0·01 and 0·1. The velocity field for flow through curved pipes of non-uniform cross-section is compared with the corresponding results for flow through straight pipes of non-uniform radius and curved pipes of uniform radius, revealing important qualitative differences. The basic developments presented are applicable to a variety of flows in pipes, including those in arteries and piping systems.

KEY WORDS curved pipe flow; variable cross-section; secondary flow; artery

1. INTRODUCTION

In this paper we consider steady, laminar flow of an incompressible Newtonian fluid in curved pipes of non-uniform cross-section. The related problem of viscous fluid flow in curved pipes of constant circular cross-section has been of considerable interest to researchers analytically, numerically and experimentally since the 1920s. In 1927 Dean published the first analytical solution for fully developed, laminar flow of a Newtonian fluid in pipes of infinitesimally small curvature ratio and constant cross-section at small Dean number. The Dean number is generally defined as the product of the Reynolds number, based on some mean axial velocity, and the square root of the ratio of the radius of the pipe cross-section to the constant radius of curvature of the pipe centreline. Dean's results were obtained by considering a perturbation of flow in a straight pipe[1,2] for small curvature ratio. Interest in obtaining analytical solutions to this problem for a larger range of Dean number has continued. For example, Green *et al.*[3] utilized a direct theory for viscous flow in pipes[4] to obtain solutions for fully developed flow in curved pipes of constant cross-section. During the past decade, researchers have taken advantage of the increase in available computing power to obtain numerical solutions to this problem over a large range of curvature ratio and Dean number (such as those obtained by Yang and Keller[5] and Soh and Berger[6]). Background information and further references on this subject can be found in books by Pedley[7] and Ward-Smith[8] and in review articles by Berger *et al.*[9] and Itō.[10]

The aforementioned results have been confined mainly to fully developed flow in pipes of uniform cross-section. This work, however, deals with flow in curved pipes of variable cross-section in order to

CCC 0271–2091/96/080771–28

Received 14 April 1994
Revised 6 July 1995

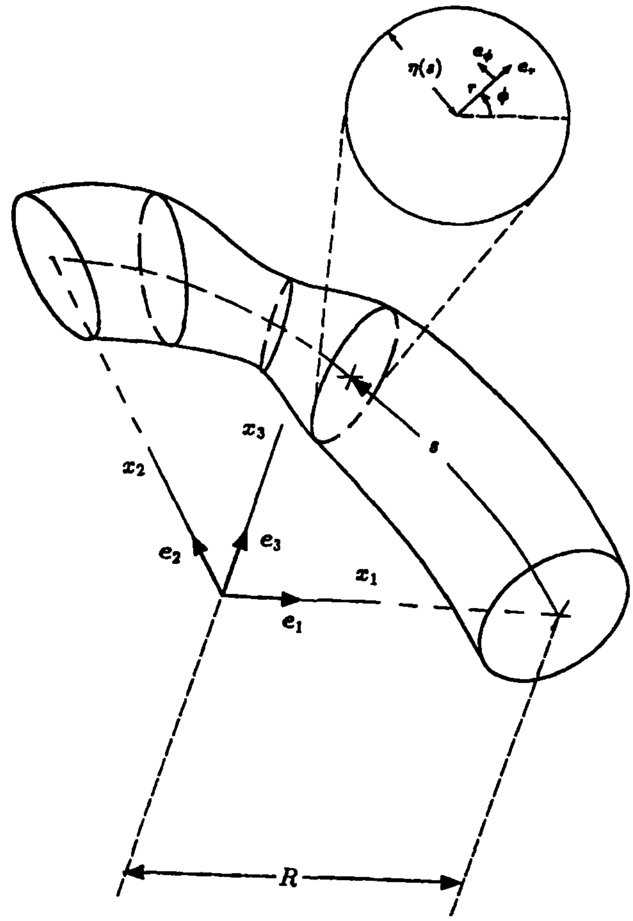

Figure 1. Segment of a pipe of variable cross-section showing its centreline (broken curve) which forms an arc of constant radius R. Also shown are the orthonormal bases $\underline{e}_i$ and the corresponding rectangular co-ordinates x_i. The inner surface of the pipe, $r=\eta(s)$, and the bases $\underline{e}_r$, $\underline{e}_\phi$ and $\underline{e}_s$ are labelled for a cross-section at axial location s

study the coupled effects of variable diameter and pipe curvature ratio on the flow field. For the case of flow through pipes of variable cross-section the velocity field is necessarily a function of the axial location along the pipe centreline as well as the two cross-sectional co-ordinates. Hence the problem cannot be formulated in terms of two spatial variables, greatly increasing the complexity and size of the numerical problem over that of fully developed flow.

The basic equations used in this study are the Navier–Stokes equations for an incompressible Newtonian fluid which are summarized in Section 2. These equations are subsequently written in non-dimensional form with respect to toroidal co-ordinates (r, ϕ, s) (Figure 1). Given a toroidal co-ordinate system (r, ϕ, s), the pipe centreline can be identified with the curve defined by r equal to zero. A longitudinal section of pipe can then be identified by specifying a constant value of circumferential angle ϕ. In Figure 2 we consider such a segment mapped into the r–s plane and identify the class of flows considered here. In particular we consider flows for which there is a transition region due to the variable radius, labelled II in Figure 2, between two regions (I and III) of fully developed flow. In the course of analysis it becomes necessary to identify the extent of the transition region II. The point on the centreline separating regions I and II will be regarded as the point at which the flow ceases to be fully

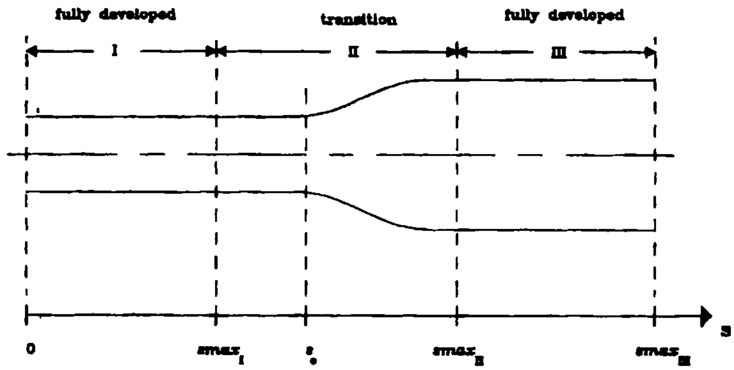

Figure 2. Schematic diagram representing a two-dimensional section of the curved pipe defined by equations (4) for fixed angle ϕ and drawn in the r–s plane. Indicated are three flow regions, two for fully developed flow and one, labelled II, which is not necessarily fully developed

developed. Similarly, the point between regions II and III will be taken as the point at which the flow commences to be fully developed.

In Section 3 we discuss the numerical procedures used to obtain a discrete approximation to the differential equations of motion and the methodology used for solving the resulting system of non-linear algebraic equations. The staggered grid system used in the numerical formulation is defined and the discrete approximations to the differential equations of motion for points on the grid are introduced. We choose the toroidal co-ordinate system, introduced above and further discussed in Section 2, because it is especially convenient for the analysis of flow in curved pipes. However, it should be emphasized that for this co-ordinate system care is needed in the numerical formulation of the equations of motion at points in the vicinity of the centreline, since at the centreline the toroidal co-ordinate system exhibits singular behaviour. We introduce a method for developing consistent discrete approximations to the equations of motion in this region. A discussion of the procedure used to solve the resulting system of non-linear algebraic equations is then provided. Section 4 contains results obtained using the numerical procedures described in Section 3. Velocity fields and the extent of the flow transition region for the case of flow through a curved pipe of non-uniform cross-section are compared with corresponding results for flow through both straight pipes of non-uniform radius and curved pipes of constant cross-section.

This work has applications to blood flow in curved sections of the arterial system where the cross-section of the artery is non-uniform. This variation in radius can be due, for example, to atherosclerosis (see e.g. Reference 11) or to a mismatch in elastic properties between an artery and arterial graft.[12] In addition, this work has industrial applications to flow in curved pipes which are non-uniform owing to material deposits on the pipe walls. Our results provide insights into the strong coupling between the effects of pipe curvature and of non-uniform cross-section in these systems.

2. FORMULATION OF THE PROBLEM

The local form of the condition of incompressibility and the equations of linear momentum for steady flow of an incompressible, homogeneous Newtonian fluid referred to rectangular Cartesian co-ordinates are

$$v_{i,i} = 0, \tag{1}$$

$$\rho v_{i,j} v_j = -p_{,i} + \mu v_{i,jj}, \tag{2}$$

where v_i are the components of velocity vector $\underset{\sim}{v}$, p is the Lagrange multiplier arising from the incompressibility constraint, ρ is the constant mass density, μ is the shear viscosity, the notation $(\ )_{,i}$ denotes $\partial(\ )/\partial x_i$ and repeated indices imply summation over the values of the index ($i = 1, 2, 3$).

We now introduce a toroidal co-ordinate system (r, ϕ, s) with respect to rectangular Cartesian co-ordinates x_i through the relations (see Figure 1)

$$r = \sqrt{\{x_3^2 + [\sqrt{(x_1^2 + x_2^2)} - R]^2\}}, \qquad \phi = \tan^{-1}\left(\frac{x_3}{\sqrt{(x_1^2 + x_2^2)} - R}\right), \qquad s = R\tan^{-1}\left(\frac{x_2}{x_1}\right) \tag{3}$$

and the inverse relations

$$x_1 = (R + r\cos\phi)\cos\frac{s}{R}, \qquad x_2 = (R + r\cos\phi)\sin\frac{s}{R}, \qquad x_3 = r\sin\phi. \tag{4}$$

Any point in Euclidean 3-space can be specified by a position vector $\underset{\sim}{r} = x_j \underset{\sim}{e}_j$, which using (4) can be written as

$$\begin{aligned} \underset{\sim}{r} &= (R + r\cos\phi)\cos\frac{s}{R}\underset{\sim}{e}_1 + (R + r\cos\phi)\sin\frac{s}{R}\underset{\sim}{e}_2 + r\sin\phi\underset{\sim}{e}_3 \\ &= (r + R\cos\phi)\underset{\sim}{e}_r - R\sin\phi\underset{\sim}{e}_\phi, \end{aligned} \tag{5}$$

where $\underset{\sim}{e}_r$ and $\underset{\sim}{e}_\phi$ are defined as

$$\underset{\sim}{e}_r = \cos\phi\left(\cos\frac{s}{R}\underset{\sim}{e}_1 + \sin\frac{s}{R}\underset{\sim}{e}_2\right) + \sin\phi\underset{\sim}{e}_3, \qquad \underset{\sim}{e}_\phi = -\sin\phi\left(\cos\frac{s}{R}\underset{\sim}{e}_1 + \sin\frac{s}{R}\underset{\sim}{e}_2\right) + \cos\phi\underset{\sim}{e}_3. \tag{6}$$

Using (6) and $\underset{\sim}{e}_s$ defined by

$$\underset{\sim}{e}_s = -\sin\frac{s}{R}\underset{\sim}{e}_1 + \cos\frac{s}{R}\underset{\sim}{e}_2, \tag{7}$$

we obtain the orthonormal basis $(\underset{\sim}{e}_r, \underset{\sim}{e}_\phi, \underset{\sim}{e}_s)$.

We consider flow through curved pipes of circular cross-section for which the inner radius of the pipe, designated $r = \hat{\eta}(s)$, is of the form

$$r = \hat{\eta}(s) = \begin{cases} a, & 0 \leqslant s \leqslant s_o, \\ a + a\alpha\{1 - 1/[1 + (s/a - s_o/a)^\gamma]\}, & s_o \leqslant s, \end{cases} \tag{8}$$

where s_o, α and γ are pipe geometry parameters which will be specified in Section 4. As can be seen in (8), at axial locations where s is less than or equal to s_o the inner wall of the pipe has radius a. The pipe surface defined in (8) includes the degenerative case of a pipe of constant radius, i.e. $\alpha = 0$.

As mentioned in Section 1, we confine attention to a class of flows which are steady, namely the pressure and velocity field are independent of time. The flow rate, designated Q, is defined through the relationship

$$Q = \int_A \underset{\sim}{v}\cdot\underset{\sim}{n}\, d\bar{a}, \tag{9}$$

where $\underset{\sim}{n}$ is the outward unit normal to the surface A and $d\bar{a}$ is a temporary notation used to denote a differential area. The flow rate is constant for steady flow of an incompressible fluid in a pipe, independent of both time and spatial variables. We use this result to define a characteristic velocity W by

$$W = \frac{Q}{\pi a^2}, \tag{10}$$

where, as defined in (8), a is the radius of the pipe at axial locations where s is less than or equal to s_o. We also recall definitions for three non-dimensional variables, the Reynolds number Re, the pipe curvature ratio δ and the Dean number κ defined as

$$Re = \frac{\rho W a}{\mu}, \qquad \delta = \frac{a}{R}, \qquad \kappa = 2Re\sqrt{\delta}. \tag{11}$$

Using the characteristic velocity defined in (10), we introduce the following non-dimensional quantities designated by the '$\sim$' notation:

$$\begin{aligned} &\tilde{s} = \frac{s}{a}, \qquad \tilde{r} = \frac{r}{a}, \qquad \tilde{\eta} = \frac{\eta}{a}, \\ &\tilde{u} = \frac{\underline{v}\cdot\underline{e}_r}{W}, \qquad \tilde{v} = \frac{\underline{v}\cdot\underline{e}_\phi}{W}, \qquad \tilde{w} = \frac{\underline{v}\cdot\underline{e}_s}{W}, \qquad \tilde{p} = \frac{p}{\rho W^2}. \end{aligned} \tag{12}$$

We use (8) and (12) to obtain

$$\tilde{\eta} = \begin{cases} 1, & 0 \leqslant \tilde{s} \leqslant \tilde{s}_0, \\ 1 + \alpha\{1 - 1/[1 + (\tilde{s} - \tilde{s}_0)^\gamma]\}, & \tilde{s}_0 \leqslant \tilde{s}, \end{cases} \tag{13}$$

where $\tilde{s} = s/a$ and $\tilde{s}_0 = s_0/a$. We then use these non-dimensional quantities to obtain the non-dimensional form of the equation of incompressibility and the $\underline{e}_r$, $\underline{e}_\phi$ and $\underline{e}_s$ components of the equations of motion (dropping the '$\sim$' notation in this and future equations):

$$0 = \frac{\partial(urB)}{\partial r} + \frac{\partial(vB)}{\partial \phi} + r\frac{\partial w}{\partial s}, \tag{14}$$

$$\begin{aligned} &u\frac{\partial u}{\partial r} + \frac{v}{r}\frac{\partial u}{\partial \phi} + \frac{w}{B}\frac{\partial u}{\partial s} - \frac{v^2}{r} - \frac{\delta w^2 \cos\phi}{B} \\ &= -\frac{\partial p}{\partial r} + \frac{1}{Re}\left[\frac{\partial^2 u}{\partial r^2} + \frac{\partial u}{\partial r}\left(\frac{1}{r} + \frac{\delta\cos\phi}{B}\right) + \frac{1}{r^2}\frac{\partial^2 u}{\partial \phi^2} - \frac{\delta\sin\phi}{rB}\frac{\partial u}{\partial \phi}\right. \\ &\left. + \frac{1}{B^2}\frac{\partial^2 u}{\partial s^2} - \frac{1}{r^2}\left(2\frac{\partial v}{\partial \phi} + u\right) + \delta\frac{v\sin\phi}{rB} + \delta\frac{\cos\phi}{B^2}\left(\delta v\sin\phi - \delta u\cos\phi - 2\frac{\partial w}{\partial s}\right)\right], \end{aligned} \tag{15}$$

$$\begin{aligned} &u\frac{\partial v}{\partial r} + \frac{v}{r}\frac{\partial v}{\partial \phi} + \frac{w}{B}\frac{\partial v}{\partial s} + \frac{uv}{r} + \frac{\delta w^2 \sin\phi}{B} \\ &= -\frac{1}{r}\frac{\partial p}{\partial \phi} + \frac{1}{Re}\left[\frac{\partial^2 v}{\partial r^2} + \frac{\partial v}{\partial r}\left(\frac{1}{r} + \frac{\delta\cos\phi}{B}\right) + \frac{1}{r^2}\frac{\partial^2 v}{\partial \phi^2}\right. \\ &\left. - \frac{\delta\sin\phi}{rB}\frac{\partial v}{\partial \phi} + \frac{1}{B^2}\frac{\partial^2 v}{\partial s^2} + \frac{1}{r^2}\left(2\frac{\partial u}{\partial \phi} - v\right) - \delta\frac{u\sin\phi}{rB} - \delta\frac{\sin\phi}{B^2}\left(\delta v\sin\phi - \delta u\cos\phi - 2\frac{\partial w}{\partial s}\right)\right], \end{aligned} \tag{16}$$

$$\begin{aligned} &u\frac{\partial w}{\partial r} + \frac{v}{r}\frac{\partial w}{\partial \phi} + \frac{w}{B}\frac{\partial w}{\partial s} + \frac{\delta w}{B}(u\cos\phi - v\sin\phi) \\ &= -\frac{1}{B}\frac{\partial p}{\partial s} + \frac{1}{Re}\left[\frac{\partial^2 w}{\partial r^2} + \frac{\partial w}{\partial r}\left(\frac{1}{r} + \frac{\delta\cos\phi}{B}\right) + \frac{1}{r^2}\frac{\partial^2 w}{\partial \phi^2}\right. \\ &\left. - \frac{\delta\sin\phi}{rB}\frac{\partial w}{\partial \phi} + \frac{1}{B^2}\frac{\partial^2 w}{\partial s^2} - \frac{2\delta}{B^2}\left(-\frac{\partial u}{\partial s}\cos\phi + \frac{\partial v}{\partial s}\sin\phi + \delta\frac{w}{2}\right)\right], \end{aligned} \tag{17}$$

where $B = 1 + \delta r\cos\phi$.

Before closing this section, we make some remarks about the choice of non-dimensional variables used in (12). In studies of flows which are not fully developed, a velocity profile may be specified at a cross-section and a characteristic velocity can then be obtained. In our developments we specify a velocity profile at $s=0$ and define the characteristic velocity to be $Q/\pi a^2$, where Q is obtained using the specified velocity profile and equation (9). In contrast, for the case of fully developed flow a velocity profile is not specified at any cross-section, hence an alternative choice of characteristic velocity is used. In this case the velocity vector is independent of the axial variable and as a result the axial component of the pressure gradient $\partial p/\partial s$ is constant. This constant value, frequently denoted $-G$ in the literature, is sometimes used to define non-dimensional velocity components (see e.g. Reference 3) as

$$\left(\frac{v_{(1)}}{W_o}, \frac{v_{(2)}}{W_o}, \frac{v_{(3)}}{W_o}\right), \tag{18}$$

where $W_o = a^2 G/8\mu$. Other authors, e.g. Dennis[13] and Daskopoulos and Lenhoff,[14] use an alternative definition of non-dimensional velocity components, namely

$$\left(v_{(1)}\frac{a}{\nu}, v_{(2)}\frac{a}{\nu}, v_{(3)}\frac{a\sqrt{(2\delta)}}{\nu}\right). \tag{19}$$

We emphasize that the non-dimensionalization in (19) is such that the limiting case of $\delta=0$ does not correspond to a straight pipe but rather to a pipe of small curvature ratio. For our purposes we employ the non-dimensional variables defined in equation (12), since this choice enables us to include the limiting case of non-fully developed flow in straight pipes in our analysis.

As was discussed in Section 1, we consider flows for which there is a transition region due to the variable radius, labelled II, between two regions of fully developed flow which are respectively labelled I and III. Figure 2 shows a schematic diagram of these three flow regimes. The point on the centreline located at the beginning of region I is defined to be s equal to zero. The point labelled $smax_{\mathrm{I}}$ in Figure 2 is the point on the centreline at which the flow ceases to be fully developed and separates regions I and II. Similarly, $smax_{\mathrm{II}}$ is the point at which the flow commences to be fully developed and separates regions II and III. The point labelled $smax_{\mathrm{III}}$ denotes the end of region III. Also shown in this figure is the point s_o which denotes the axial location at which the pipe radius begins to increase from the constant value a to a second radius $a(1+\alpha)$ as indicated by (8). We consider flows which are symmetric about the plane $x_3=0$ (see Figure 1), for which case

$$u(r,\phi,s)=u(r,-\phi,s), \qquad v(r,\phi,s)=-v(r,-\phi,s), \qquad w(r,\phi,s)=w(r,-\phi,s). \tag{20}$$

As a result of the flow symmetry (20), we choose the domain of the fluid to be that bounded by the surface $x_3=0$ and the lateral surface of the pipe, $r=\eta(s)$. The upstream and downstream boundaries on the flow are the planes perpendicular to the centreline of the pipe, passing through the points s equal to zero and to $smax_{\mathrm{III}}$. On the lateral surface we specify the no-slip boundary condition, namely

$$\hat{\underline{v}}(\hat{\eta}(s),\phi,s)=0. \tag{21}$$

It is clear from (20) that

$$v(r,0,s)=v(r,\pi,s)=0. \tag{22}$$

As will be further elaborated on in Section 3, we specify a fully developed velocity profile, denoted $\underline{v}_o$, at the beginning of region I, i.e.

$$\underline{v}(r,\phi,0)=\hat{\underline{v}}_o(r,\phi), \tag{23}$$

and specify that the flow be fully developed at $s = smax_{\rm III}$, namely

$$\frac{\partial v}{\partial s}(r, \phi, smax_{\rm III}) = 0. \tag{24}$$

In the equations of motion (1) and (2) the pressure p occurs only in the term $p_{,i}$, namely as operated on by the gradient operator. The pressure field is therefore determined as part of the solution up to an additive constant. Equations (14)–(17) in conjunction with conditions (20)–(24) and the condition on the pressure field constitute the formulation of the problem under consideration.

3. NUMERICAL PROCEDURES

As in Reference 15, where laminar entrance flow in a curved pipe of constant cross-section is studied, we use a non-uniform staggered grid for our finite difference formulation.

3.1. Non-uniform grid

For the pipe flow under discussion it is clear at the outset that the flow field has the simplest dependence on the spatial variable s in flow regimes I and III (where the flow is fully developed) as well as in areas of flow regime II bordering regimes I and III. We therefore define a co-ordinate mapping $\bar{s} = \bar{s}(s)$ such that points separated by a constant distance $\bar{s} = \Delta\bar{s}$ correspond to a grid of points which is least dense in areas of the flow field just mentioned. We use the co-ordinate mapping $\bar{s} = \bar{s}(s)$ defined through the invertible relationship

$$s = \hat{s}(\bar{s}) = A\left[\frac{E}{4}\sin(2\bar{s} + 2C) + \bar{s}\left(1 + \frac{E}{2}\right)\right] + D, \tag{25}$$

where constants A and D are chosen such that the domain $\bar{s} \in [0, \overline{smax}_{\rm III}]$ corresponds to the domain $s \in [0, smax_{\rm III}]$. E is non-negative and constants E, C and $\overline{smax}_{\rm III}$ are chosen dependent on both the pipe surface geometry and the flow parameters as will be discussed in Section 4.

In order to simplify the discrete form of the no-slip condition (21) at numerical grid points corresponding to the lateral boundary of the pipe, we define the new independent variable $\bar{r}$ through the invertible relation

$$\bar{r} = \frac{r}{\hat{\eta}(s)}, \tag{26}$$

where the surface $\bar{r} = 1$ coincides with the surface $r = \eta(s)$.

It is clear from (25) and (26) that dependent variables which are functions of (r, ϕ, s) can be written as functions of $(\bar{r}, \phi, \bar{s})$. For example, a function $\hat{f}(r, \phi, s)$ can be written as

$$f = \hat{f}(r, \phi, s) = \bar{f}(\bar{r}, \phi, \bar{s}) \tag{27}$$

and therefore

$$\frac{\partial \hat{f}}{\partial r} = \frac{1}{\eta}\frac{\partial \bar{f}}{\partial \bar{r}}, \qquad \frac{\partial \hat{f}}{\partial s} = \frac{1}{s'}\frac{\partial \bar{f}}{\partial \bar{s}} - \beta\frac{\partial \bar{f}}{\partial \bar{r}}, \tag{28}$$

where η', s' and β stand for

$$\eta' = \frac{d\hat{\eta}(s)}{ds}, \qquad s' = \frac{d\hat{s}(\bar{s})}{d\bar{s}}, \qquad \beta = \bar{\beta}(\bar{r}, \bar{s}) = \frac{\bar{r}\eta'}{\eta}. \tag{29}$$

Table I. Notation used for the staggered grid system

Grid label	Grid symbol	Discrete operator	Corresponding location of grid points	Total number of grid points
p	●	$p_{[i,j,k]}$	$(\bar{r}, \phi, \bar{s}) = (r2_i, \phi 1_j, s1_k)$ $(i = 1, 2, \dots, L; j = 1, 2, \dots, M; k = 1, 2, \dots, N)$	LMN
p	●	$p'_{[k]}$	Centreline $(x_1^2 + x_2^2 = R^2, x_3 = 0)$: $\bar{s} = s1_k$ $(k = 1, 2, \dots, N-1)$	$N-1$
u	○	$u_{[i,j,k]}$	$(\bar{r}, \phi, \bar{s}) = (r1_i, \phi 1_j, s1_k)$ $(i = 1, 2, \dots, L; j = 1, 2, \dots, M; k = 1, 2, \dots, N)$	LMN
v	▲	$v_{[i,j,k]}$	$(\bar{r}, \phi, \bar{s}) = (r1_i, \phi 2_j, s1_k)$ $(i = 1, 2, \dots, L; j = 1, 2, \dots, M-1; k = 1, 2, \dots, N)$	$L(M-1)N$
w	△	$w_{[i,j,k]}$	$(\bar{r}, \phi, \bar{s}) = (r1_i, \phi 1_j, s2_k)$ $(i = 1, 2, \dots, L; j = 1, 2, \dots, M; k = 1, 2, \dots, N-1)$	$LM(N-1)$

Using (25)–(29), we can rewrite the non-dimensional form of the equations of motion (14)–(17) with respect to spatial variables $(\bar{r}, \phi, \bar{s})$. These equations are not included here but can be found in Reference 16.

3.2. *Staggered grid*

We define approximations to the continuous functions $p(\bar{r}, \phi, \bar{s})$, $u(\bar{r}, \phi, \bar{s})$, $v(\bar{r}, \phi, \bar{s})$ and $w(\bar{r}, \phi, \bar{s})$ on a staggered grid, i.e. the four discrete functions are defined on four *different* grids. Schematics of these grids are denoted by ●, ○, ▲ and △ in Figure 3 and will be referred to as the p, u, v and w grids respectively. For example, the discrete function which is an approximation to $u(\bar{r}, \phi, \bar{s})$ is defined on a three-dimensional grid composed of points designated (i, j, k), where $i = 1, 2, \dots, L$, $j = 1, 2, \dots, M$ and $k = 1, 2, \dots, N$. This grid, which we call the u grid, corresponds to points designated by the symbol ○ in Figure 3, where we have introduced $r1_i$, $r2_i$, $\phi 1_j$, $\phi 2_j$, $s1_k$ and $s2_k$ as

$$\begin{aligned} r1_i &= (i - \tfrac{1}{2})\Delta\bar{r}, \qquad & \phi 1_j &= (j - \tfrac{1}{2})\Delta\phi, \qquad & s1_k &= (k - \tfrac{1}{2})\Delta\bar{s}, \\ r2_i &= i\Delta\bar{r}, & \phi 2_j &= j\Delta\phi, & s2_k &= k\Delta\bar{s}. \end{aligned} \tag{30}$$

We use the notation $u_{[i,j,k]}$ to denote the discrete function which is an approximation to the continuous function $u(\bar{r}, \phi, \bar{s})$ at the point $(r1_i, \phi 1_j, s1_k)$. Similar notation is used to identify points on the p, v and w grids and is summarized in Table I.

We use the following notational scheme to indicate the values of functions B, η and β at points on the staggered grid:

$$\begin{aligned} &B1_{[i,j,k]} = \bar{B}(r1_i, \phi 1_j, s1_k), \quad B2_{[i,j,k]} = \bar{B}(r2_i, \phi 1_j, s1_k), \quad B3_{[i,j,k]} = \bar{B}(r1_i, \phi 2_j, s1_k), \\ &B4_{[i,j,k]} = \bar{B}(r2_i, \phi 2_j, s1_k), \quad B5_{[i,j,k]} = \bar{B}(r1_i, \phi 1_j, s2_k), \quad B6_{[i,j,k]} = \bar{B}(r2_i, \phi 1_j, s2_k), \\ &\beta 1_{[i,k]} = \bar{\beta}(r1_i, s1_k), \quad \beta 2_{[i,k]} = \bar{\beta}(r2_i, s1_k), \quad \beta 3_{[i,k]} = \bar{\beta}(r1_i, s2_k), \\ &\beta 4_{[i,k]} = \bar{\beta}(r2_i, s2_k), \quad \eta 1_{[k]} = \bar{\eta}(s1_k), \quad \eta 2_{[k]} = \bar{\eta}(s2_k). \end{aligned} \tag{31}$$

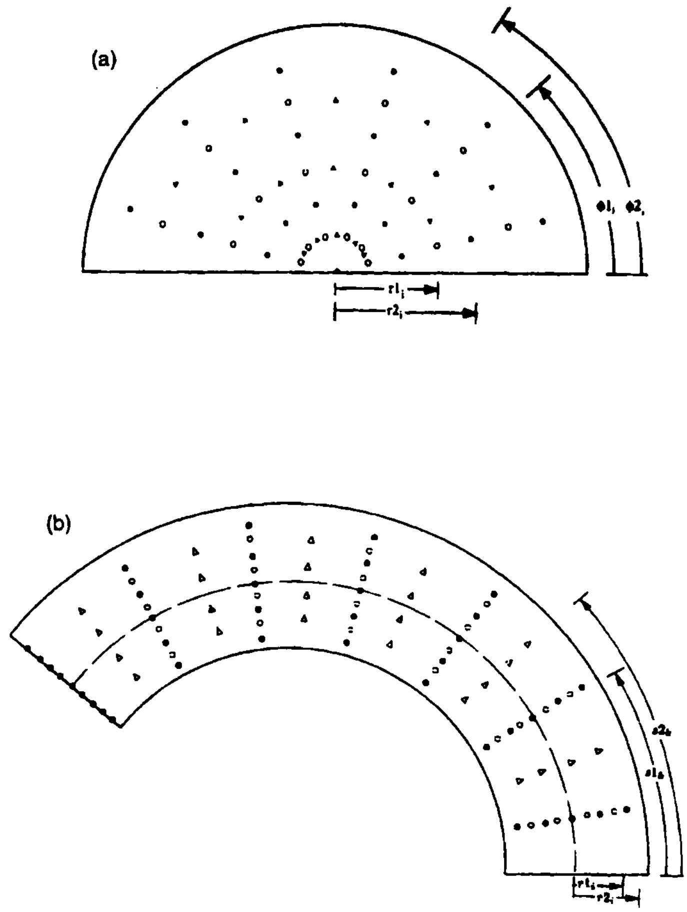

Figure 3. Schematic of the computational grid system. As described in Section 3.2, the p, u, v and w grids are denoted by ●, ○, ▲ and △ respectively. In (a) the p, u and v grids are drawn for fixed axial location $s = s1_k$. Similarly, in (b) the p, u and w grids are displayed for fixed angle $\phi = \phi 1_j$

Owing to the nature of a staggered grid, it is necessary to interpolate the discrete function on a given grid to obtain approximate values of this discrete function at points on a different grid. The notation used to denote these interpolations is defined in Table II.

The discrete form of the no-slip boundary condition (21) is

$$u_{[L+1,j,k]} = v_{[L+1,j,k]} = w_{[L+1,j,k]} = 0 \tag{32}$$

and the discrete condition corresponding to (23) can be written as

$$u_{[i,j,0]} = \underline{v}_0(r1_i, \phi 1_j)\cdot \underline{e}_r, \qquad v_{[i,j,0]} = \underline{v}_0(r1_i, \phi 2_j)\cdot \underline{e}_\phi, \qquad w_{[i,j,0]} = \underline{v}_0(r1_i, \phi 1_j)\cdot \underline{e}_s. \tag{33}$$

A second-order approximation for the fully developed flow condition (24) takes the form

$$u_{[i,j,N+1]} = u_{[i,j,N]}, \qquad v_{[i,j,N+1]} = v_{[i,j,N]}, \qquad w_{[i,j,N]} = w_{[i,j,N-1]}. \tag{34}$$

Using conditions (20) and (22) and the staggered grid notation just defined, we obtain symmetry conditions for the discrete operators, namely

Table II. Definition of discrete operators used to approximate a function f at points on the staggered grid

Notation for discrete operator	Definition of discrete operator	Order of accuracy of approximation
$\overset{r}{\bar{f}}_{[i,j,k]}$	$\dfrac{f_{[i+1,j,k]}+f_{[i,j,k]}}{2}$	Second
$\overset{\phi}{\bar{f}}_{[i,j,k]}$	$\dfrac{f_{[i,j+1,k]}+f_{[i,j,k]}}{2}$	Second
$\overset{2\phi}{\bar{f}}_{[i,j,k]}$	$\dfrac{-f_{[i,j+2,k]}+9f_{[i,j+1,k]}+9f_{[i,j,k]}-f_{[i,j-1,k]}}{16}$	Fourth
$\overset{s}{\bar{f}}_{[i,j,k]}$	$\dfrac{f_{[i,j,k+1]}+f_{[i,j,k]}}{2}$	Second

$$\begin{aligned} &u_{[i,0,k]} = u_{[i,1,k]}, && v_{[i,0,k]} = 0, && w_{[i,0,k]} = w_{[i,1,k]}, \\ &u_{[i,-1,k]} = u_{[i,2,k]}, && v_{[i,-1,k]} = -v_{[i,1,k]}, && w_{[i,-1,k]} = w_{[i,2,k]} \end{aligned} \tag{35}$$

and

$$\begin{aligned} &u_{[i,M+1,k]} = u_{[i,M,k]}, && u_{[i,M+2,k]} = u_{[i,M-1,k]}, && v_{[i,M,k]} = 0, \\ &v_{[i,M+1,k]} = -v_{[i,M-1,k]}, && w_{[i,M+1,k]} = w_{[i,M,k]}, && w_{[i,M+2,k]} = w_{[i,M-1,k]}. \end{aligned} \tag{36}$$

The above particular conditions (35) and (36) are sufficient symmetry conditions for the numerical formulation. As discussed at the beginning of this section, for the formulation of this problem we specify a value of the pressure p at one point in the fluid domain. For our purposes we specify the pressure to be zero at a point on the centreline of the pipe corresponding to $\bar{s}=s1_N$, i.e. $p'_{[N]}=0$.

As discussed in Section 2, the equations of motion (14)–(17) can be written with respect to spatial variables ($\bar{r}$, ϕ, $\bar{s}$). We replace the differential operators in the resulting equations by the finite difference operators summarized in Table III to obtain the following second-order finite difference approximations to the equations of motion:

$$\begin{aligned} 0 = {} & D_{1r}[u_{[i,j,k]}B1_{[i,j,k]}r1_{[i]}] + D_{1\phi}[\overset{r}{\bar{v}}_{[i,j-1,k]}\overset{r}{\bar{B}}3_{[i,j-1,k]}] \\ & + r2_{[i]}\eta 1_{[k]}\left(\frac{1}{s1'_{[k]}}D_{1s}[\overset{r}{\bar{w}}_{[i,j,k-1]}] - \beta 2_{[i,k]}D_{1r}[\overset{s}{\bar{w}}_{[i,j,k-1]}]\right), \end{aligned} \tag{37}$$

$$\begin{aligned} & \frac{u_{[i,j,k]}}{\eta 1_{[k]}}D_{2r}[u_{[i,j,k]}] + \frac{\overset{2\phi}{\bar{v}}_{[i,j-1,k]}}{r1_{[i]}\eta 1_{[k]}}D_{4\phi}[u_{[i,j,k]}] - \frac{(\overset{2\phi}{\bar{v}}_{[i,j-1,k]})^2}{r1_{[i]}\eta 1_{[k]}} \\ & + \frac{\overset{s}{\bar{w}}_{[i,j,k-1]}}{B1_{[i,j,k]}}\left(\frac{1}{s1'_{[k]}}D_{2s}[u_{[i,j,k]}] - \beta 1_{[i,k]}D_{2r}[u_{[i,j,k]}]\right) - \frac{\delta\cos\phi 1_{[j]}}{B1_{[i,j,k]}}(\overset{s}{\bar{w}}_{[i,j,k-1]})^2 \end{aligned}$$

Table III. Definition of discrete operators used to approximate the continuous differential operators

Notation for discrete operator	Definition of discrete operator	Corresponding continuous operator	Order of accuracy of approximation
$D_{1r}(f_{[i,j,k]})$	$\dfrac{f_{[i+1,j,k]}-f_{[i,j,k]}}{\Delta\bar{r}}$	$\partial f/\partial\bar{r}$	Second
$D_{2r}(f_{[i,j,k]})$	$\dfrac{f_{[i+1,j,k]}-f_{[i-1,j,k]}}{2\Delta\bar{r}}$	$\partial f/\partial\bar{r}$	Second
$D_{3r}(f_{[i,j,k]})$	$\dfrac{-f_{[i+2,j,k]}+8f_{[i+1,j,k]}-8f_{[i-1,j,k]}+f_{[i-2,j,k]}}{12\Delta\bar{r}}$	$\partial f/\partial\bar{r}$	Fourth
$D_{rr}(f_{[i,j,k]})$	$\dfrac{f_{[i+1,j,k]}+f_{[i-1,j,k]}-2f_{[i,j,k]}}{\Delta\bar{r}^2}$	$\partial^2 f/\partial\bar{r}^2$	Second
$D_{1\phi}(f_{[i,j,k]})$	$\dfrac{f_{[i,j+1,k]}-f_{[i,j,k]}}{\Delta\phi}$	$\partial f/\partial\phi$	Second
$D_{2\phi}(f_{[i,j,k]})$	$\dfrac{f_{[i,j+1,k]}-f_{[i,j-1,k]}}{\Delta\phi}$	$\partial f/\partial\phi$	Second
$D_{3\phi}(f_{[i,j,k]})$	$\dfrac{f_{[i,j-1,k]}-27f_{[i,j,k]}+27f_{[i,j+1,k]}-f_{[i,j+2,k]}}{24\Delta\phi}$	$\partial f/\partial\phi$	Fourth
$D_{4\phi}(f_{[i,j,k]})$	$\dfrac{f_{[i,j-2,k]}+8f_{[i,j-1,k]}+8f_{[i,j+1,k]}-f_{[i,j+2,k]}}{12\Delta\phi}$	$\partial f/\partial\phi$	Fourth
$D_{\phi\phi}(f_{[i,j,k]})$	$\dfrac{-f_{[i,j-2,k]}+16f_{[i,j-1,k]}-30f_{[i,j,k]}+16f_{[i,j+1,k]}-f_{[i,j+2,k]}}{12\Delta\phi^2}$	$\partial^2 f/\partial\phi^2$	Fourth
$D_{1s}(f_{[i,j,k]})$	$\dfrac{f_{[i,j,k+1]}-f_{[i,j,k]}}{\Delta s}$	$\partial f/\partial\bar{s}$	Second
$D_{2s}(f_{[i,j,k]})$	$\dfrac{f_{[i,j,k+1]}-f_{[i,j,k-1]}}{2\Delta s}$	$\partial f/\partial\bar{s}$	Second
$D_{ss}(f_{[i,j,k]})$	$\dfrac{f_{[i,j,k+1]}+f_{[i,j,k-1]}-2f_{[i,j,k]}}{\Delta\bar{s}^2}$	$\partial^2 f/\partial\bar{s}^2$	Second
$D_{rs}(f_{[i,j,k]})$	$\dfrac{f_{[i+1,j,k+1]}-f_{[i+1,j,k-1]}-f_{[i-1,j,k+1]}+f_{[i-1,j,k-1]}}{4\Delta\bar{r}\Delta s}$	$\partial^2 f/\partial\bar{r}\partial\bar{s}$	Second

$$
\begin{aligned}
&= -\frac{1}{\eta 1_{[k]}} D_{1r}[p_{[i-1,j,k]}] + \frac{1}{Re}\Bigg\{ \frac{1}{(\eta 1_{[k]} r 1_{[i]})^2} D_{rr}[u_{[i,j,k]}] \\
&+ D_{3r}[u_{[i,j,k]}]\left(\frac{1}{r 1_{[i]} \eta 1^2_{[k]}} + \frac{\delta \cos \phi 1_{[j]}}{\eta 1_{[k]} B 1_{[i,j,k]}}\right) \\
&+ \frac{1}{(r 1_{[i]} \eta 1_{[k]})^2} D_{\phi\phi}[u_{[i,j,k]}] - \frac{\delta \sin \phi 1_{[j]}}{r 1_{[i]} \eta 1_{[k]}} D_{4\phi}[u_{[i,j,k]}] \\
&+ \frac{1}{B 1^2_{[i,j,k]}} \Bigg[\frac{1}{s 1'^{2}_{[k]}} D_{ss}[u_{[i,j,k]}] - \frac{s 1''_{[k]}}{s 1'^{3}_{[k]}} D_{2s}[u_{[i,j,k]}] - 2 \frac{\beta 1_{[i,k]}}{s 1'_{[k]}} D_{rs}[u_{[i,j,k]}] \\
&+ D_{2r}[u_{[i,j,k]}]\left(\frac{2 \beta 1_{[i,k]} \eta 1'_{[k]}}{\eta 1_{[k]}} - \frac{r 1_{[i]} \eta 1''_{[k]}}{\eta 1_{[k]}}\right) + \beta 1^2_{[i,k]} D_{rr}[u_{[i,j,k]}] \Bigg] \\
&- \frac{1}{r 1^2_{[i]} \eta 1^2_{[k]}} \left(2 D_{3\phi}[v_{[i,j-1,k]}] + u_{[i,j,k]}\right) + \overset{2\phi}{\bar{v}}_{[i,j-1,k]} \Bigg(\frac{\delta \sin \phi 1_{[j]}}{B 1_{[i,j,k]} r 1_{[i]} \eta 1_{[k]}} \\
&+ \frac{\delta^2 \cos \phi 1_{[j]} \sin \phi 1_{[j]}}{B 1^2_{[i,j,k]}} \Bigg) - \frac{\delta^2 \cos^2 \phi 1_{[j]}}{B 1^2_{[i,j,k]}} u_{[i,j,k]} - \frac{2\delta \cos \phi 1_{[j]}}{B 1^2_{[i,j,k]}} \Bigg(\frac{1}{s 1'_{[k]}} D_{1s}[w_{[i,j,k-1]}] \\
&- \beta 1_{[i,k]} D_{2r}[\overset{s}{\bar{w}}_{[i,j,k-1]}] \Bigg) \Bigg\},
\end{aligned}
\tag{38}
$$

$$
\begin{aligned}
&\frac{\overset{2\phi}{\bar{u}}_{[i,j,k]}}{\eta 1_{[k]}} D_{2r}[v_{[i,j,k]}] + \frac{v_{[i,j,k]}}{r 1_{[i]} \eta 1_{[k]}} D_{4\phi}[v_{[i,j,k]}] - \frac{\overset{2\phi}{\bar{u}}_{[i,j,k]} v_{[i,j,k]}}{r 1_{[i]} \eta 1_{[k]}} \\
&+ \frac{1}{B 3_{[i,j,k]}} \frac{\overset{\phi}{\bar{w}}_{[i,j+1,k]} + \overset{\phi}{\bar{w}}_{[i,j,k-1]}}{2} \left(\frac{1}{s 1'_{[k]}} D_{2s}[v_{[i,j,k]}] - \beta 1_{[i,k]} D_{2r}[v_{[i,j,k]}] \right) \\
&+ \frac{\delta \sin \phi 2_{[j]}}{B 3_{[i,j,k]}} \left(\frac{\overset{\phi}{\bar{w}}_{[i,j+1,k]} + \overset{\phi}{\bar{w}}_{[i,j,k-1]}}{2} \right)^2 \\
&= -\frac{1}{\eta 1_{[k]} r 1_{[i]}} D_{3\phi}[p_{[i,j,k]}] + \frac{1}{Re} \Bigg\{ \frac{1}{\eta 1^2_{[k]}} D_{rr}[v_{[i,j,k]}] \\
&+ D_{3r}[v_{[i,j,k]}] \left(\frac{1}{r 1_{[i]} \eta 1^2_{[k]}} + \frac{\delta \cos \phi 2_j}{\eta 1_{[k]} B 3_{[i,j,k]}} \right) \\
&+ \frac{1}{(r 1_{[i]} \eta 1_{[k]})^2} D_{\phi\phi}[v_{[i,j,k]}] - \frac{\delta \sin \phi 2_j}{r 1_{[i]} \eta 1_{[k]}} D_{4\phi}[v_{[i,j,k]}]
\end{aligned}
$$

$$
\begin{aligned}
&+\frac{1}{B3^2_{[i,j,k]}}\Bigg[\frac{1}{s1'^{\,2}_{[k]}}D_{ss}[v_{[i,j,k]}]-\frac{s1''_{[k]}}{s1'^{\,3}_{[k]}}D_{2s}[v_{[i,j,k]}]-2\frac{\beta 1_{[i,k]}}{s1'_{[k]}}D_{rs}[v_{[i,j,k]}]\\
&+D_{2r}[v_{[i,j,k]}]\left(\frac{2\beta 1_{[i,k]}\eta 1'_{[k]}}{\eta 1_{[k]}}-\frac{r1_{[i]}\eta 1''_{[k]}}{\eta 1_{[k]}}\right)+\beta 1^2_{[i,k]}D_{rr}[v_{[i,j,k]}]\Bigg]\\
&+\overset{2\phi}{\bar{u}}_{[i,j,k]}\left(\frac{-\delta\sin\phi 2_j}{B3_{[i,j,k]}r1_{[i]}\eta 1_{[k]}}+\frac{\delta^2\cos\phi 2_j\sin\phi 2_j}{B3^2_{[i,j,k]}}\right)-v_{[i,j,k]}\frac{\delta^2\sin^2\phi 2_j}{B3^2_{[i,j,k]}}\\
&-\frac{2\delta\sin\phi 2_j}{B3^2_{[i,j,k]}}\left(\frac{1}{s1'_{[k]}}D_{1s}[\overset{\phi}{\bar{w}}_{[i,j,k-1]}]-2\beta 1_{[ik]}D_{2r}\left[\frac{w_{[i,j+1,k]}+w_{[i,j,k-1]}}{2}\right]\right)\Bigg\},
\end{aligned}
\tag{39}
$$

$$
\begin{aligned}
&\frac{\overset{s}{\bar{u}}_{[i,j,k]}}{\eta 2_{[k]}}D_{2r}[w_{[i,j,k]}]+\frac{1}{r1_{[i]}\eta 2_{[k]}}\frac{v_{[i,j,k+1]}+v_{[i,j-1,k]}}{2}D_{4\phi}[w_{[i,j,k]}]\\
&\quad+\frac{w_{[i,j,k]}}{B5_{[i,j,k]}}\left(\frac{1}{s2'_{[k]}}D_{2s}[w_{[i,j,k]}]-\beta 3_{[i,k]}D_{2r}[w_{[i,j,k]}]\right)\\
&\quad-\frac{\delta w_{[i,j,k]}}{B5_{[i,j,k]}}\left(\overset{s}{\bar{u}}_{[i,j,k]}\cos\phi 1_j-\frac{v_{[i,j,k+1]}+v_{[i,j-1,k]}}{2}\sin\phi 1_j\right)\\
&=-\frac{1}{B5_{[i,j,k]}}\left(\frac{1}{s2'_{[k]}}D_{1s}[\overset{r}{\bar{p}}_{[i-1,j,k]}]-\beta 2_{[i,k]}D_{1r}[\overset{s}{\bar{p}}_{[i-1,j,k]}]\right)\\
&\quad+\frac{1}{Re}\Bigg\{\frac{1}{\eta 2^2_{[k]}}D_{rr}[w_{[i,j,k]}]+D_{3r}[w_{[i,j,k]}]\left(\frac{1}{r1_{[i]}\eta 2^2_{[k]}}+\frac{\delta\cos\phi 1_j}{\eta 2_{[k]}B5_{[i,j,k]}}\right)\\
&\quad+\frac{D_{\phi\phi}[w_{[i,j,k]}]}{(r1_{[i]}\eta 2_{[k]})^2}-\frac{\delta\sin\phi 1_j}{r1_{[i]}\eta 2_{[k]}}D_{4\phi}[w_{[i,j,k]}]\\
&\quad+\frac{1}{B5^2_{[i,j,k]}}\Bigg[\frac{1}{s2'_{[k]}2}D_{ss}[w_{[i,j,k]}]-\frac{s2''_{[k]}}{s2'_{[k]}3}D_{2s}[w_{[i,j,k]}]-2\frac{\beta 3_{[i,k]}}{s2'_{[k]}}D_{rs}[w_{[i,j,k]}]\\
&\quad+D_{2r}[w_{[i,j,k]}]\left(\frac{2\beta 3_{[i,k]}\eta 2'_{[k]}}{\eta 2_{[k]}}-\frac{r1_{[i]}\eta 2''_{[k]}}{\eta 2_{[k]}}\right)+\beta 3^2_{[i,k]}D_{rr}[w_{[i,j,k]}]\Bigg]\\
&\quad+\frac{2\delta}{B5^2_{[i,j,k]}}\Bigg(\frac{1}{s2'_{[k]}}D_{1s}[u_{[i,j,k]}\cos\phi 1_j-\beta 3_{[i,k]}D_{2r}[\overset{s}{\bar{u}}_{[i,j,k]}]\cos\phi 1_j\\
&\quad+D_{1s}[\overset{\phi}{\bar{v}}_{[i,j-1,k]}]\frac{\sin\phi 1_j}{s2'_{[k]}}-\beta 3_{[i,k]}\sin\phi 1_j D_{2r}\left[\frac{v_{[i,j,k+1]}+v_{[i,j-1,k]}}{2}\right]+\frac{\delta}{2}w_{[i,j,k]}\Bigg)\Bigg\}.
\end{aligned}
\tag{40}
$$

These equations are defined on the p, u, v and w grids respectively with the following exceptions. As will be discussed in the next subsection, equation (37) is not used for points on the p grid which correspond to the centreline of the pipe. In addition, the operators D_{2r}, D_{rr} and D_{rs} defined in Table III will not be used at grid points adjacent to the centreline.

3.3. *Pipe centreline*

It is clear from (3) that ϕ is undefined on the centreline of the pipe, $x_1^2+x_2^2=R^2$, $x_3=0$. Consequently, neither orthonormal base vector $\underline{e}_r$ nor $\underline{e}_\phi$ is defined on this curve and hence neither is the velocity component u nor v. This characteristic of the toroidal co-ordinate system has three important implications for our finite difference formulation.

1. At points near the centreline the value of the radial variable r is of order Δr, so care must be taken in formulating the finite difference approximations to maintain the order of accuracy of the approximation.
2. The incompressibility condition (1) is not defined on the centreline when written in component form relative to toroidal co-ordinates (r, ϕ, s).
3. At points adjacent to the centreline the finite difference approximations D_{2r}, D_{rr} and D_{rs} defined in Tables III are not valid.

These results, which are due to the singular nature of the toroidal co-ordinate system (r, ϕ, s) on the centreline,* are independent of the physics of the problem.

Terms in the equations of motion with coefficients $1/\bar{r}$ and $1/\bar{r}^2$ must be approximated carefully near the centreline where $\bar{r}$ is of the order of $\Delta\bar{r}$. For example, the differential operator in the term $(1/\bar{r})\partial u/\partial\phi$ must be approximated by a third-order finite difference approximation in order for the entire expression to be an approximation with error of the order of $\Delta\bar{r}^2$. To simplify the numerical formulation, we use the higher-order approximation for the underlined terms at all grid points.

Equation (37) cannot be used as the discrete approximation to (1) at points on the p grid corresponding to points on the centreline, because the incompressibility condition in terms of velocity components relative to co-ordinates (r, ϕ, s) is undefined on the centreline. As outlined in Appendix I and further described in Reference 16, at grid points corresponding to points on the pipe centreline we use curvilinear co-ordinates which are well defined throughout the flow domain to obtain a valid second-order-accurate approximation for the incompressibility condition (1). This co-ordinate system is chosen such that the resulting finite difference approximation can be written as a function of the discrete functions $u_{[i,j,k]}$ and $w_{[i,j,k]}$ and is of the form

$$\begin{aligned}0=&\frac{1}{\eta 1_k\Delta\bar{r}}(u_{[1,1,k]}+u_{[1,M,k]}+u_{[1,M/2+1,k]}+u_{[1,M/2,k]})\\&+\frac{1}{8\Delta\bar{s}}(w_{[1,1,k]}+w_{[1,M,k]}-w_{[1,1,k-1]}-w_{[1,M,k-1]})\\&-\frac{\delta\sin\phi 1_1}{2}(u_{[1,M/2+1,k]}-u_{[1,M/2,k]})+\frac{\delta\cos\phi 1_1}{2}(u_{[1,1,k]}-u_{[1,M,k]}).\end{aligned}\tag{41}$$

The discrete equation (41) is a well-defined second-order finite difference approximation to the incompressibility condition (1) for p grid points corresponding to points on the centreline of the pipe.

* Recall that we chose the curvilinear co-ordinate system (r, ϕ, s) because of other desirable properties. For example, after a simple co-ordinate transformation defined at the beginning of this section, equation (26), co-ordinate lines defined by $\bar{r}=1$ coincide with the inner wall of the pipe.

Owing to the singular nature of the toroidal co-ordinate system (r, ϕ, s) at the centreline of the pipe, certain conditions necessary for the approximations $D_{2r}(f_{[i,j,k]})$, $D_{rr}(f_{[i,j,k]})$ and $D_{rs}(f_{[i,j,k]})$, defined in Table III, to be valid are not met at grid points adjacent to the centreline. This problem arises even though the partial derivatives $\partial f/\partial\bar{r}$, $\partial^2 f/\partial\bar{r}^2$ and $\partial^2 f/\partial\bar{r}\partial\bar{s}$ are well defined at these grid points for a function f equivalent to u, v or w. In Appendix II we obtain a valid discrete approximation for $\partial v/\partial r$ at points adjacent to the centreline by making use of the same curvilinear co-ordinates as introduced in Appendix I. We used a similar approach to obtain the discrete approximations which are used to replace the operators $D_{2r}(f_{[i,j,k]})$, $D_{rr}(f_{[i,j,k]})$ and $D_{rs}(f_{[i,j,k]})$ in (37)–(40) at grid points adjacent to the centreline.

We use Newton's method (see e.g. Reference 17) to solve the system of equations (37)–(40) and (41) with corresponding grid boundary conditions (32)–(36) including the condition on $p'_{[N]}$. To simplify this discussion, we first introduce the vector $\underline{y}$ where the components of $\underline{y}$ are the values of the discrete functions $u_{[i,j,k]}$, $v_{[i,j,k]}$, $w_{[i,j,k]}$, $p_{[i,j,k]}$ and $\underline{p}'_{[k]}$ at points on the staggered grid system. As can be seen in Table I, the total number of grid points, the sum of column 5, is $4LMN - LN - LM + N - 1$. Similarly, we introduce the discrete vector function $\underline{g}$ such that the components of $\underline{g}$ are equal to the left side of the finite difference equations (37)–(40) and (41); namely, using the notation just introduced, the system of finite difference equations can be written in the form

$$g_i = \hat{g}_i(y_j) = 0, \tag{42}$$

where $i, j = 1, 2, \ldots, 4LMN - LN - LM + N - 1$. In the application of Newton's method to the system of equations (42), a sequence of iterative solutions y_i^n is defined through the relations

$$\frac{\partial \hat{g}_i(\underline{y}^n)}{\partial y_j}\Delta y_j^n = -\hat{g}_i(\underline{y}^n) \tag{43}$$

for $i, j = 1, 2, \ldots, 4LMN - LN - LM + N - 1$ and $n = 0, 1, 2, \ldots,$ where

$$\Delta y_j^n = y_j^{n+1} - y_j^n \tag{44}$$

and y_i^0 is the initial estimate of y_i. We stop the iterative process when

$$|y_i^{n+1} - y_i^n| < \varepsilon \tag{45}$$

for all i, where we use ε to 1×10^{-5}. In order to obtain solutions y_i to (43), we make use of two sparse matrix packages which employ direct methods (see e.g. Reference 18). We use a combination of sparse matrix routines F04AXF, F01BRf and F01BSF from the NAG library,* which employ a sparse variation of Gaussian elimination with pivoting for the solution of large sparse matrix equations. For denser grid studies (larger systems of equations) we make use of the SMPAK† mathematical library, which includes routines that use Gaussian elimination without pivoting to solve large sparse matrices.

4. RESULTS AND DISCUSSION

4.1. Details of the numerical formulation for specific studies

As discussed earlier and shown in Figure 2, the flow field is fully developed in regions I and III. For a numerical study we must specify the downstream boundary of region III (identified by the axial value

* NAG, the Numerical Algorithms Group (originally the Nottingham Algorithms Group), develops and distributes a library of mathematical routines.

† SMPAK is a commercial release of the Yale Sparse Matrix Package, sold and supported by Scientific Computing Associates Inc.

$smax_{\mathrm{III}}$) *a priori* and then check the numerical solution to ascertain that this value is large enough so that the discrete solution for the flow field is fully developed in some appropriate discrete sense at the upstream and downstream limits of the numerical domain. To facilitate the discussion, we restrict our attention to one component of the velocity field, namely the radial component. Since the pipe is of constant radius in the two regions under discussion, we define the radial velocity component to be fully developed in a discrete sense at the axial location corresponding to $s2_k$ if

$$\frac{1}{s1'_{[k]}}\frac{u_{[i,j,k]}-u_{[i,j,k-1]}}{\Delta\bar{s}}<\varepsilon \tag{46}$$

for all $i = 1, 2, \ldots, L$ and $j = 1, 2, \ldots, M$, where ε was defined in Section 3 following equation (45). It may be emphasized that ε is the upper bound on the magnitude of the update for the final iteration of Newton's method and is therefore a measure of accuracy of the numerical solution. With this in mind we define the value of $smax_{\mathrm{I}}$ for our numerical studies to be the smallest value of the arc length s such that the discrete approximation to the fully developed condition (46) is met throughout the cross-section for all components of velocity as well as for $\partial p/\partial s$. Similarly, we define the value of $smax_{\mathrm{II}}$ as the smallest value of the arc length s such that s is greater than s_o and the discrete approximation to the fully developed condition is met for all components of velocity as well as for $\partial p/\partial s$ throughout the cross-section.

We obtain this fully developed velocity profile $\underline{v}_o$ introduced in equation (23) by solving the system of discrete equations (37)–(40) for flow through a curved pipe of constant cross-section ($\alpha = 0{\cdot}0$) with grid conditions (32), (34) and (35), $p'_{[N]}$ equal to zero and the non-dimensional velocity field at $\bar{s}=0$ specified as

$$u_{[i,j,0]}=v_{[i,j,0]}=0, \qquad w_{[i,j,0]}=(1{\cdot}0-r^2)/2{\cdot}0, \tag{47}$$

namely Poiseuille flow. As is discussed in Reference 9, other velocity profiles have also been used when studying developing flow in curved pipes of constant cross-section. This choice does not directly affect our analysis, because we use it only as a means to obtain the fully developed velocity field $\underline{v}_o$.*

The constants C, E and $\overline{smax}$ introduced in the co-ordinate mapping $s=\bar{s}(\bar{s})$ in (25) are chosen to concentrate the grid points in regions where the flow is most complex. For the pipe geometries considered in this work, we use C equal to $\pi/8$ and $\overline{smax}$ equal to $11\pi/8$. The value of E is chosen dependent on Reynolds number and curvature ratio.

The computations necessary to solve the system of linear equations (43) were carried out on a CRAY Y-MP/864 at the University of California at San Diego and a CRAY Y-MP/832 at the Pittsburgh Supercomputing Center. A typical numerical study on the CRAY Y-MP/864 using the SMPAK subroutine TDRV required five iterations of Newton's method for the convergence criterion (45) to be met. For a staggered grid of dimension $(L, M, N)=(10, 12, 15)$, approximately 500 s of CPU time were used per iteration. The corresponding Jacobian matrix $\partial g_i/\partial y_j$ introduced in equation (43) was of order 6944 and contained 185,773 non-zero elements. It was necessary to allocate 15·3 Mwords of storage when using the SMPAK subroutine TDRV to solve equation (43) for this case.

4.2. Results obtained for flow in curved pipes of non-constant cross-section

Three categories of plots are used to display the velocity field. In the first category of plots we consider a longitudinal section of pipe mapped onto the r–s plane. The radial and axial components of the velocity vector $u\underline{e}_r + w\underline{e}_s$ are drawn in this plane; see e.g. Figure 8. In the second and third categories

* Note that we could also obtain the profile $\underline{v}_o$ by considering a formulation in which the equations of motion have been specialized for fully developed flow, a problem involving only two independent variables; see e.g. Reference 5.

of plots, e.g. Figures 9 and 10, we consider pipe cross-sections at various locations along the pipe centreline defined by specified values of arc length s. Contours of constant axial velocity w are displayed in the second category of plots, while for the third category the radial and circumferential components of the velocity at these cross-sections are plotted as the in-plane velocity vector $u\underline{e}_r + v\underline{e}_\phi$ (often referred to as the secondary flow). It is important to note that these figures are shown at different scales. For comparison, a relative scaling value is indicated in the corresponding captions. These three categories of plots are systematically depicted in Figures 4–14 and are shown for a Reynolds number equal to 25·0 and curvature ratios equal to 0·0, 0·01 and 0·1. All non-uniform cross-section results are for the pipe geometry parameters $\gamma = 6{\cdot}0$ and $\alpha = 0{\cdot}5$.

Specifically, consider Figures 7–10 which display velocity fields for $Re = 25{\cdot}0$ and $\delta = 0{\cdot}01$. The plot in Figure 7 corresponds to a longitudinal pipe section defined by x_3 equal to zero, while that in Figure 8 corresponds to a longitudinal pipe section perpendicular to the x_1–x_2 plane and intersecting the pipe centreline. Shown in the upper left and right sections of both these figures are magnifications of two sections of the in-plane velocity profile at the axial location $s/a = 17{\cdot}5$. Owing to the symmetry of the flows under consideration, the two enlarged profiles in Figure 8 are mirror images of each other. They have been drawn for comparison with Figure 7, in which the profiles are not related in this way. Figure 9 shows contours of constant axial velocity w corresponding to increasing values of non-dimensional arc length s/a. Similarly, Figure 10 displays the radial and circumferential components of the velocity at cross-sections for increasing values of s/a. Owing to the nature of the staggered grid, the second category of plots corresponds to pipe cross-sections located at axial positions between those for the third category of plots.

Displayed in Table IV are values of $smax_{\mathrm{I}}$, $smax_{\mathrm{II}}$, $smax_{\mathrm{III}}$ and the corresponding subtended angle (in degrees), where this angle θ is defined as

$$\theta = \delta \frac{180^\circ}{\pi} \frac{s}{a}. \tag{48}$$

The extent of the flow transition region, namely the difference between $smax_{\mathrm{II}}$ and $smax_{\mathrm{I}}$, is shown in Table V over a range of Reynolds numbers and curvature ratios. Also shown are the quantities

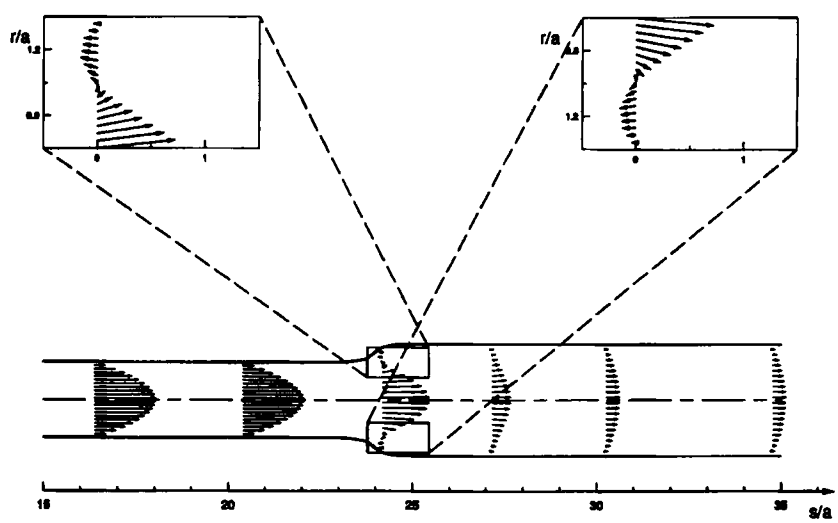

Figure 4. Two components of the velocity vector $u\underline{e}_r + w\underline{e}_s$ for a longitudinal section of pipe and shown in the r–s plane for $Re = 25{\cdot}0$ and $\delta = 0{\cdot}0$ (straight pipe). Profiles are drawn at axial positions $s/a = 16{\cdot}4$, $20{\cdot}4$, $24{\cdot}8$, $27{\cdot}2$, $30{\cdot}3$ and $34{\cdot}8$. Also shown are enlargements of two sections of a profile at $s/a = 24{\cdot}2$

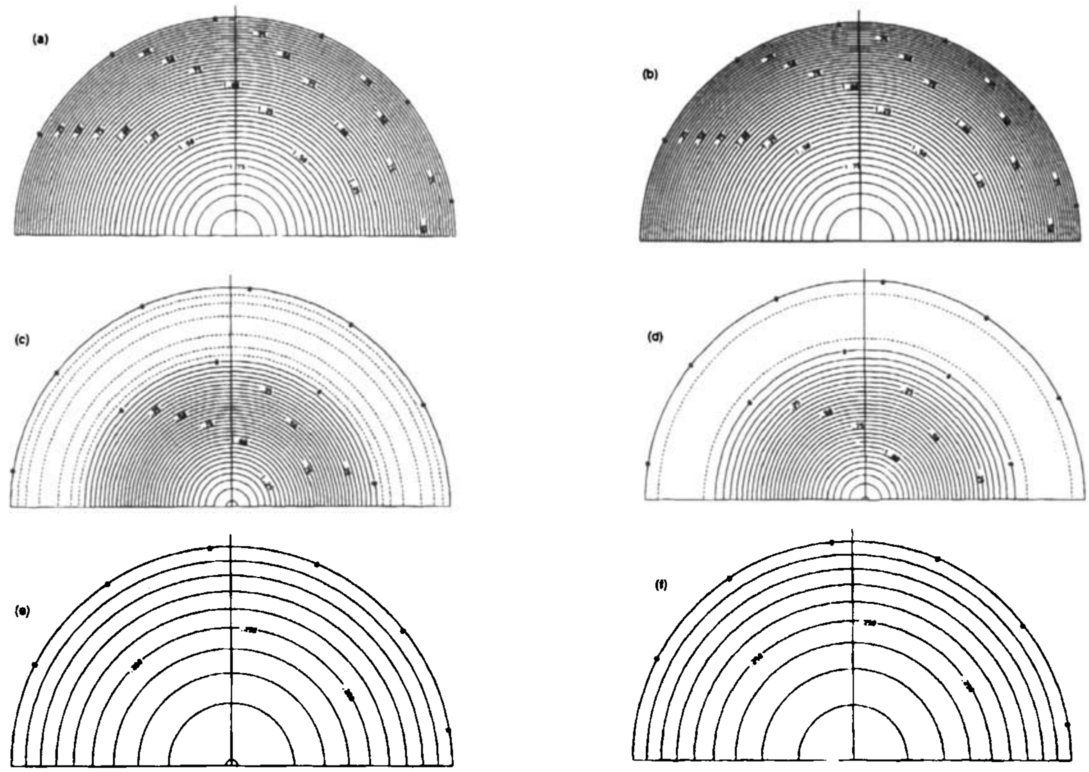

Figure 5. Contours of constant axial velocity w for the pipe cross-section at arc length s/a equal to (a) 5·4, (b) 20·4, (c) 24·2, (d) 24·8, (e) 30·3 and (f) 46·0 for $Re = 25{\cdot}0$ and $\delta = 0{\cdot}0$

$s_o - smax_I$ and $smax_{II} - s_o$, which designate the arc lengths of the sections of region II located upstream and downstream of s_o respectively.

In the subsequent discussion we refer to Tables IV and V and the figures just described in order to identify the three flow regimes, namely the transition region and the two regions of fully developed flow.* For example, focusing attention on the case of $Re = 25{\cdot}0$ and $\delta = 0{\cdot}01$, we see from Table IV that the region of flow transition lies between $s/a = 4{\cdot}9$ and $31{\cdot}9$ and corresponds to Figures 9(b)–9(e) and 10(b)–10(e), while Figures 9(a) and 10(a) correspond to flow regime I and Figures 9(f) and 10(f) to flow regime III.

4.3. *Discussion*

We now discuss the results for specific values of Reynolds number and curvature ratio, comparing the results obtained for flow through a curved pipe of non-uniform cross-section with those for flow through both a straight pipe of non-uniform cross-section and a curved pipe of constant cross-sectional radius.

First we focus attention on results obtained for flow in a straight pipe of non-constant cross-section, shown in Figures 4–6. The results for regions of fully developed flow display the well-known Poiseuille solution which is axisymmetric about the pipe centreline with only one non-zero component of velocity, w. The first two profiles in Figure 4 and both Figures 5(a) and 6(a) correspond to region I, namely they are drawn for axial locations upstream of $s/a = 10{\cdot}4$. As the fluid flows downstream through the

* We obtain values for $smax_I$ and $smax_{II}$ using the discrete condition for fully developed flow defined in Section 3.2.

Table IV. Results obtained for $smax_{\mathrm{I}}$, $smax_{\mathrm{II}}$ and values specified for s_o and $smax_{\mathrm{III}}$ as a function of Reynolds number and curvature ratio

δ	Re	κ	s_o/a	$smax_{\mathrm{I}}/a$	$smax_{\mathrm{II}}/a$	$smax_{\mathrm{III}}/a$
0·0	1·0	0·0	7·3	2·9	13·9	20·0
0·0	25·0	0·0	22·9	10·4	40·8	55·0
0·01	1·0	0·2	7·3 (4·2°)	2·9 (1·7°)	13·9 (8·0°)	20·0 (11·5°)
0·01	25·0	5·0	16·2 (9·3°)	4·9 (2·8°)	31·9 (18·3°)	40·0 (22·9°)
0·1	1·0	6·3	7·3 (41·8°)	2·9 (16·6°)	15·0 (85·7°)	20·0 (114·6°)
0·1	25·0	15·8	18·5 (106·0°)	2·7 (15·8°)	34·4 (197·1°)	45·0 (257·8°)

Table V. Results obtained for the extent of the transition region, $smax_{\mathrm{II}} - smax_{\mathrm{I}}$, as a function of Reynolds number and curvature ratio. Also shown are the quantities $s_o - smax_{\mathrm{I}}$ and $smax_{\mathrm{II}} - s_o$, which are the extent of this region upstream and downstream of s_o respectively

δ	Re	$(smax_{\mathrm{II}} - smax_{\mathrm{I}})/a$	$(s_o - smax_{\mathrm{I}})/a$	$(smax_{\mathrm{II}} - s_o)/a$
0·0	1·0	11·0	4·4	6·6
0·0	25·0	30·4	12·5	17·9
0·01	1·0	11·0 (6·3°)	4·4 (2·5°)	6·6 (3·8°)
0·01	25·0	27·0 (15·5°)	11·3 (6·5°)	15·7 (9·0°)
0·1	1·0	12·1 (69·3°)	4·4 (25·2°)	7·7 (44·1°)
0·1	25·0	31·7 (181·6°)	15·8 (90·5°)	15·9 (91·1°)

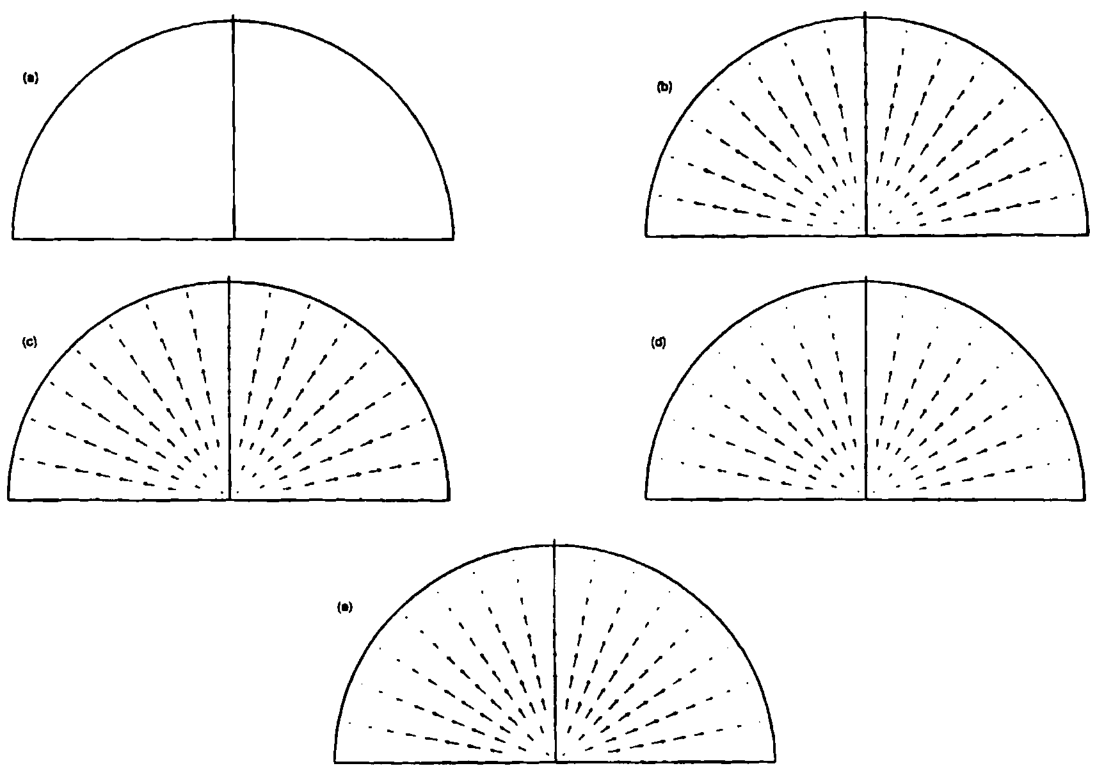

Figure 6. The in-plane velocity vector $u\underline{e}_r + v\underline{e}_\phi$ for the pipe cross-section at arc length s/a equal to (a) 0·0, (b) 18·6, (c) 23·7, (d) 24·5 and (e) 28·5 for $Re = 25·0$ and $\delta = 0·0$ for graphics scaling factor (a) 0·01, (b) 0·00045, (c) 0·01, (d) 0·1 and (e) 0·01

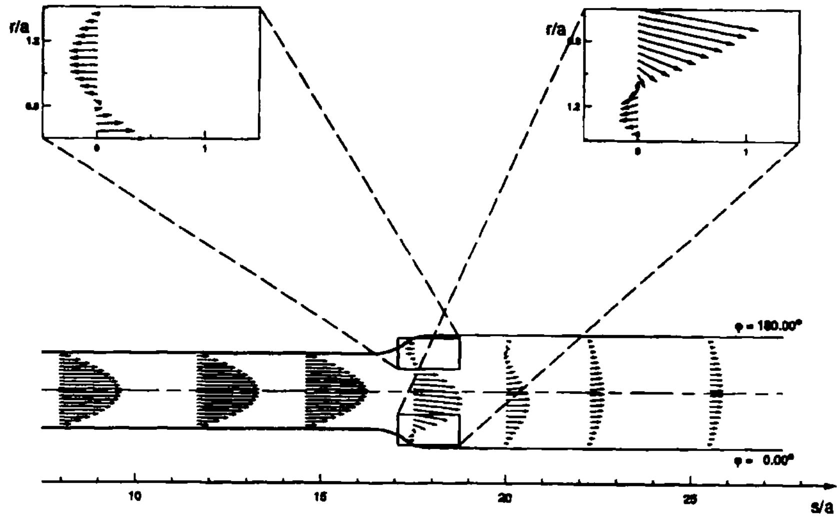

Figure 7. Two components of the velocity vector $u\underline{e}_r + w\underline{e}_s$ in the longitudinal section defined by $x_3 = 0$ and shown in the r–s plane for $Re = 25{\cdot}0$ and $\delta = 0{\cdot}01$. Profiles are drawn at axial positions $s/a = 8{\cdot}0$, $11{\cdot}7$, $14{\cdot}6$, $17{\cdot}5$, $20{\cdot}0$, $22{\cdot}3$ and $25{\cdot}5$ and the enlarged profile at $s/a = 17{\cdot}5$

transition region, the flow remains axisymmetric but develops a non-zero radial component flowing outwards towards the pipe wall, Figures 6(b)–6(e). Regions of negative axial velocity are found in parts of the transition region, as can be seen in Figure 4 (enlarged profiles) and in Figures 5(c) and 5(d), where they are drawn as dotted curves. Downstream of the transition region, i.e. s/a greater than 40·8, the flow returns to a Poiseuille profile, Figure 5(f). The velocity field in region III differs in magnitude from that in region I owing to the larger radius in region III.

We now turn attention to results for flow in curved pipes, shown in Figures 7–14. Focusing attention on pipes of curvature ratio 0·01 and flow at Reynolds number 25·0, we consider Figures 7–10. In region

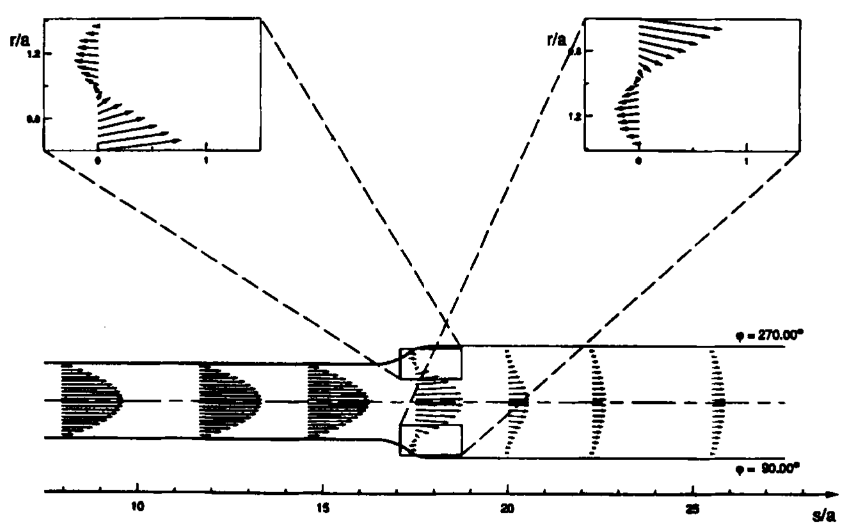

Figure 8. Two components of the velocity vector $u\underline{e}_r + w\underline{e}_s$ in the longitudinal section defined by angles $\phi = 90{\cdot}0°$ and $270°$ and shown in the r–s plane for $Re = 25{\cdot}0$ and $\delta = 0{\cdot}01$. Profiles are drawn at axial positions $s/a = 8{\cdot}0$, $11{\cdot}7$, $14{\cdot}6$, $17{\cdot}5$, $20{\cdot}0$, $22{\cdot}3$ and $25{\cdot}5$ and the enlarged profile at $s/a = 17{\cdot}5$

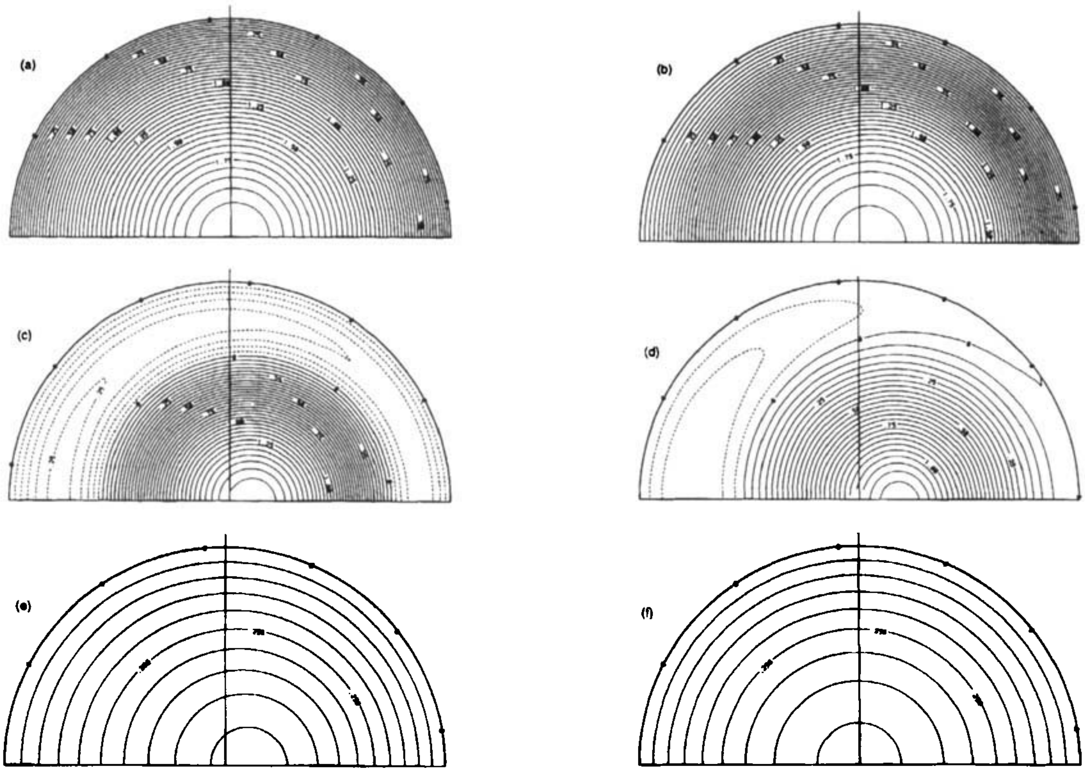

Figure 9. Contours of constant axial velocity w for the pipe cross-section at acr length s/a equal to (a) 3·9, (b) 16·5, (c) 17·5, (d) 18·7, (e) 22·3 and (f) 37·2 for $Re=25{\cdot}0$ and $\delta=0{\cdot}01$

I we find the expected results for fully developed flow in a curved pipe of circular cross-section; the contours of constant axial velocity are shifted outwards from the centre of curvature owing to centrifugal forces and are therefore asymmetric relative to the pipe centreline, Figure 9(a). A secondary flow characterized by counter-rotating vortices is found, Figure 10(a). As the fluid progresses downstream through the region of increasing cross-sectional radius, both the axial velocity contours and the secondary flow differ markedly from that in region I. The shift in the axial velocity contours outwards from the centre of the pipe becomes significantly more pronounced, Figures 9(b)–9(e). Moreover, contours of negative axial velocity (shown as dotted lines) can be seen in some sections of the transition region, Figures 9(c) and 9(d). Figure 9(c) corresponds to the middle profile in Figures 7 and 8. The negative axial velocity is clearly seen in the enlarged sections of this profile found at the top of Figures 7 and 8. Further downstream, Figure 9(e), the regions of negative axial velocity are absent and the contours of axial velocity have shifted back towards the pipe centreline. This shift continues as the flow travels downstream until it reaches region III, corresponding to the second region of fully developed flow, Figure 9(f).

We now turn attention from the contours of constant axial velocity to Figures 10(a)–10(f), which display the secondary flow fields at the same values of Reynolds number and curvature ratio just discussed. In order to contrast the secondary flow in the transition region with that in regions I and III, we refer to the vertical line drawn passing through the centreline on each of the pipe cross-sections and observe the velocity vectors along this line. In the first fully developed region, Figure 10(a), the in-plane velocity vectors at the base of this line (near the symmetry plane) are directed outwards from the centreline (towards the right of the plot). As the fluid travels downstream, the velocity vectors are seen to

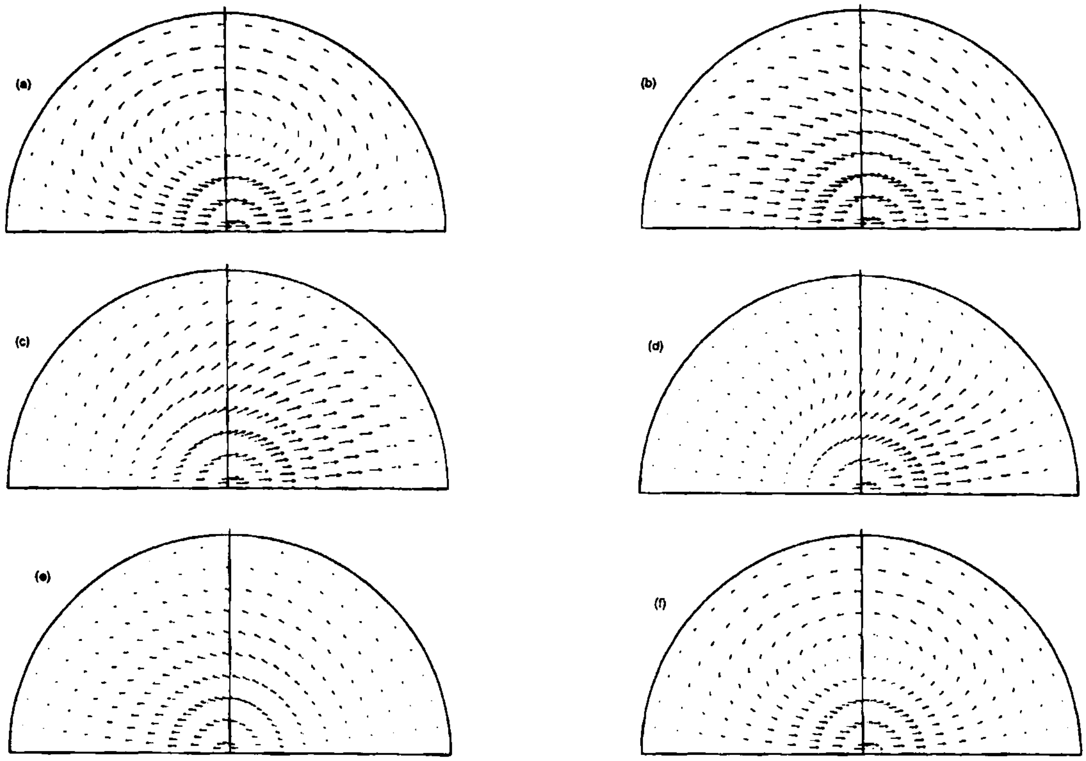

Figure 10. The in-plane velocity vector $u\underline{e}_r + v\underline{e}_\phi$ for the pipe cross-section at arc length s/a equal to (a) 0·0, (b) 15·7, (c) 17·1, (d) 18·3, (e) 21·0 and (f) 38·7 for $Re = 25{\cdot}0$ and $\delta = 0{\cdot}01$ and graphics scaling factor (a) 0·015, (b) 0·04, (c) 0·22, (d) 0·22, (e) 0·1 and (f) 0·002

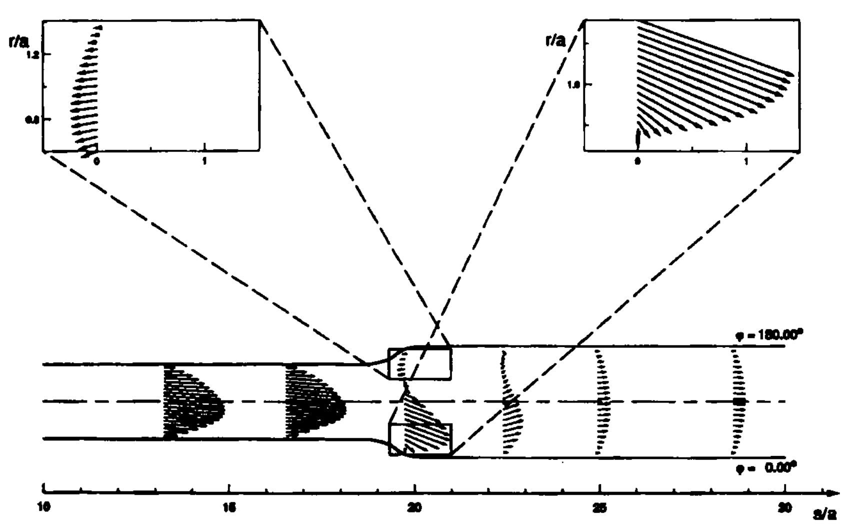

Figure 11. Two components of the velocity vector $u\underline{e}_r + w\underline{e}_s$ in the longitudinal section defined by $x_3 = 0$ and shown in the r–s plane for $Re = 25{\cdot}0$ and $\delta = 0{\cdot}1$. Profiles are drawn at axial positions $s/a = 13{\cdot}3$, 16·5, 19·7, 22·4, 24·9 and 28·2 and the enlarged profile at $s/a = 19{\cdot}7$

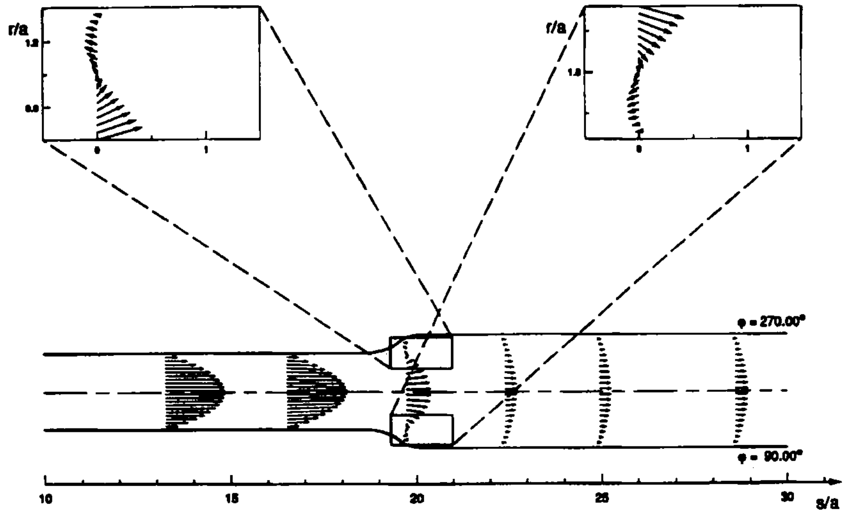

Figure 12. Two components of the velocity vector $u\underline{e}_r + w\underline{e}_s$ in the longitudinal section defined by angles $\phi = 90{\cdot}0°$ and 270° and shown in the r–s plane for $Re = 25{\cdot}0$ and $\delta = 0{\cdot}1$. Profiles are drawn at axial positions $s/a = 13{\cdot}3$, 16·5, 19·7, 22·4, 24·9 and 28·2 and the enlarged profile at $s/a = 19{\cdot}7$

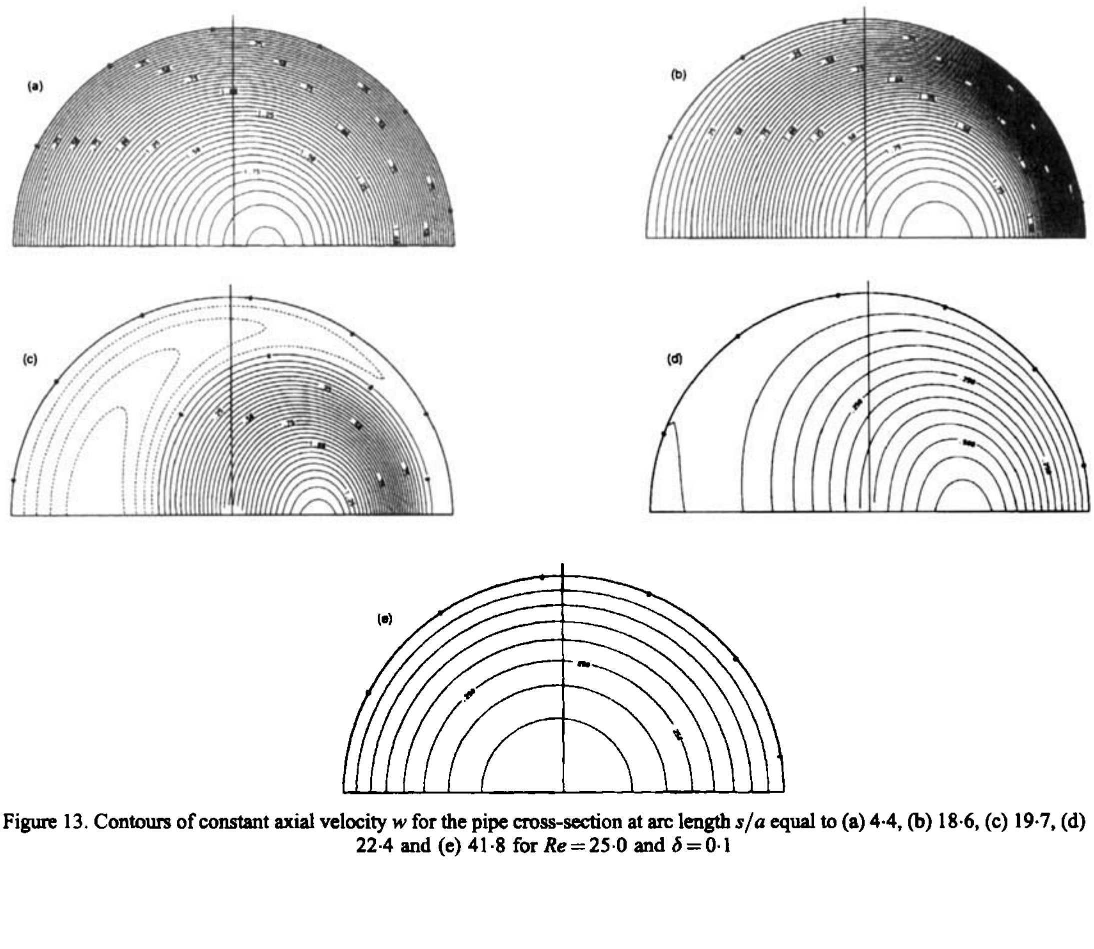

Figure 13. Contours of constant axial velocity w for the pipe cross-section at arc length s/a equal to (a) 4·4, (b) 18·6, (c) 19·7, (d) 22·4 and (e) 41·8 for $Re = 25{\cdot}0$ and $\delta = 0{\cdot}1$

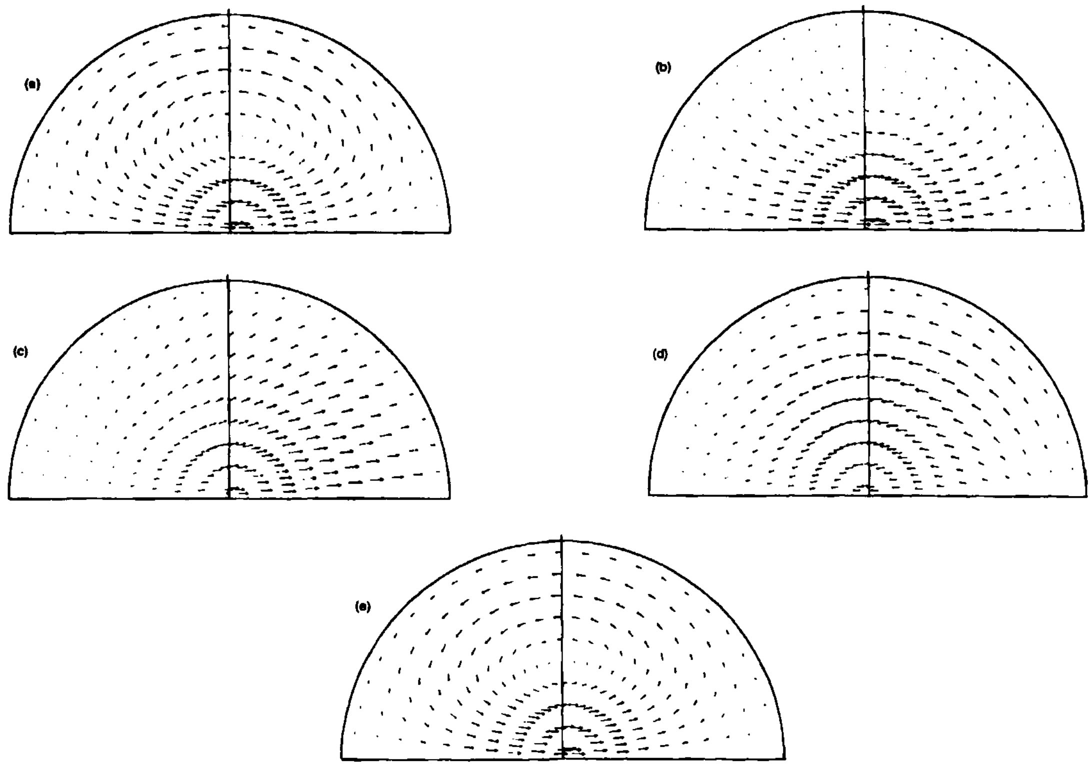

Figure 14. The in-plane velocity vector $u\underline{e}_r + v\underline{e}_\phi$ for the pipe cross-section at arc length s/a equal to (a) 0·0, (b) 17·7, (c) 19·3, (d) 21·6 and (e) 39·9 for $Re=25{\cdot}0$ and $\delta=0{\cdot}1$ for graphics scaling factor (a) 0·135, (b) 0·22, (c) 0·65, (d) 0·22 and (e) 0·0135

increase by more than a factor of 10 in magnitude, Figures 10(b)–10(d), relative to that found in region I. Further downstream, Figure 10(e), these vectors decrease in magnitude and become directed inwards from the pipe centreline. As seen in Figure 10(f), even further downstream these vectors are once again directed outwards from the centreline. Similarly, the velocity vector at points along the vertical line in the neighbourhood of the pipe boundary can also be seen to shift direction.

We consider the effect of curvature ratio on the flow field by comparing the results just discussed (for flow in pipes of curvature ratio $\delta=0{\cdot}01$) with results obtained for a pipe with curvature ratio $\delta=0{\cdot}1$, Figures 11–14. Comparing Figures 9 and 13, it can be seen that the contours of constant axial velocity for pipes of curvature ratio 0·1 are qualitatively similar to those for a pipe of curvature ratio 0·01, though the axial shift is much more dramatic for pipes of $\delta=0{\cdot}1$. In addition, at higher curvature ratios the regions of negative axial velocity occupy a larger portion of the cross-section (compare e.g. Figures 7 and 11).

We close this section with a comparison of the extent of the transition region, $smax_{\mathrm{II}} - smax_{\mathrm{I}}$, for different combinations of Reynolds number and curvature ratio. It is clear from the results shown in Table V that the extent of the transition region, written with respect to non-dimensional arc length, is strongly a function of Reynolds number and a relatively weak function of curvature ratio for the parameters considered.

Theoretical studies of flow in stenosed arteries usually do not incorporate the curvature of the pipe, considering the flow in straight pipes instead. In these cases it is assumed that the effect of pipe curvature on the flow is negligible relative to other effects such as non-uniformity of the cross-section.

However, as discussed above, the interplay of these two effects is highly non-linear, so comparing these effects separately can be misleading. We expect that the coupled effects of curvature and non-uniform pipe radius will be even more important at higher Reynolds numbers, e.g. in the range found in arterial flows.

ACKNOWLEDGEMENTS

The author would like to thank her thesis supervisor Professor P. M. Naghdi of the University of California at Berkeley for his guidance and helpful comments on this work. The author is extremely grateful for supercomputing resources provided by the Pittsburgh Supercomputing Center and the San Diego Supercomputing Center for the calculations presented here.

APPENDIX I

The purpose of this appendix is to outline the steps used to obtain a second-order-accurate valid approximation to the equation of incompressibility (1) at grid points corresponding to points on the pipe centreline. In view of this, we now introduce curvilinear co-ordinates $\bar{\alpha}^i$ which are well defined throughout the flow domain and for which co-ordinate curves intersect the staggered grid in a manner which enables us to write the finite difference approximation for the equation of incompressibility as a function of $u_{[i,j,k]}$ and $w_{[i,j,k]}$. This co-ordinate system may be defined in terms of the Cartesian co-ordinates x_i as

$$\begin{aligned}
\bar{\alpha}^1 &= \frac{1}{a\eta}\{x_3 \sin\omega + [\surd(x_1^2 + x_2^2) - R]\cos\omega\},\\
\bar{\alpha}^2 &= \frac{1}{a\eta}\{x_3 \cos\omega - [\surd(x_1^2 + x_2^2) - R]\sin\omega\},\\
\bar{\alpha}^3 &= \hat{s}^{-1}\frac{R}{a}\tan^{-1}\left(\frac{x_2}{x_1}\right)
\end{aligned} \tag{49}$$

and inverse relations

$$\begin{aligned}
x_1 &= (R + a\eta\bar{\alpha}^1\cos\omega - a\eta\bar{\alpha}^2\sin\omega)\cos\frac{as(\bar{\alpha}^3)}{R},\\
x_2 &= (R + a\eta\bar{\alpha}^1\cos\omega - a\eta\bar{\alpha}^2\sin\omega)\sin\frac{as(\bar{\alpha}^3)}{R},\\
x_3 &= a\eta(\bar{\alpha}^2\cos\omega + \bar{\alpha}^1\sin\omega),
\end{aligned} \tag{50}$$

where the function $\hat{s}(\bar{s})$ is defined in (25) and the constant angle ω will be specified later such that co-ordinate curves intersect grid lines. We introduce dimensionless velocity components u^*, v^* and w^* with respect to rectangular components of the velocity vector $v_i = \underline{v}\cdot\underline{e}_i$, as

$$\begin{aligned}
u^* &= \frac{\cos\omega}{\surd(x_1^2 + x_2^2)}(x_1 v_1 + x_2 v_2) + v_3\sin\omega,\\
v^* &= \frac{-\sin\omega}{\surd(x_1^2 + x_2^2)}(x_1 v_1 + x_2 v_2) + v_3\cos\omega,\\
w^* &= \frac{1}{\surd(x_1^2 + x_2^2)}(-x_2 v_1 + x_1 v_2).
\end{aligned} \tag{51}$$

Using (49)–(51), the incompressibility equation (1) can be written with respect to co-ordinates $\bar{\alpha}^i$ and as a function of the velocity components u^*, v^* and w^* as

$$0 = \frac{1}{\eta}\frac{\partial u^*}{\partial \bar{\alpha}^1} + \frac{1}{\eta}\frac{\partial v^*}{\partial \bar{\alpha}^2} + \left[\frac{\partial w^*}{\partial \bar{\alpha}^3}\left(\frac{\mathrm{d}\hat{s}(\bar{\alpha}^3)}{\mathrm{d}\bar{\alpha}^3}\right)^{-1} - \frac{\partial w^*}{\partial \bar{\alpha}^1}\frac{\bar{\alpha}^1}{\eta}\frac{\mathrm{d}\eta}{\mathrm{d}\bar{\alpha}^3} - \frac{\partial w^*}{\partial \bar{\alpha}^2}\frac{\bar{\alpha}^2}{\eta}\frac{\mathrm{d}\eta}{\mathrm{d}\bar{\alpha}^3} + u^*\delta\cos\omega - v^*\delta\sin\omega\right]/(1 + \bar{\alpha}^1\delta\eta\cos\omega - \bar{\alpha}^2\delta\eta\sin\omega), \tag{52}$$

which is well defined on the pipe centreline $\bar{\alpha}^1 = \bar{\alpha}^2 = 0$, where it takes the form

$$\frac{1}{\eta}\frac{\partial u^*}{\partial \bar{\alpha}^1} + \frac{1}{\eta}\frac{\partial v^*}{\partial \bar{\alpha}^2} + \frac{\partial w^*}{\partial \bar{\alpha}^3}\left(\frac{\mathrm{d}\hat{s}(\bar{\alpha}^3)}{\mathrm{d}\bar{\alpha}^3}\right)^{-1} + \delta u^*\cos\omega - \delta v^*\sin\omega. \tag{53}$$

We are now in a position to introduce a second-order finite difference approximation to (53) at the centreline as

$$\begin{aligned}0 = {} & \frac{u^*(\Delta\bar{\alpha}^1, 0, \bar{\alpha}^3) - u^*(-\Delta\bar{\alpha}^1, 0, \bar{\alpha}^3)}{2\eta\Delta\bar{\alpha}^1} + \frac{v^*(0, \Delta\bar{\alpha}^2, \bar{\alpha}^3) - v^*(0, -\Delta\bar{\alpha}^2, \bar{\alpha}^3)}{2\eta\Delta\bar{\alpha}^2} \\ & + \frac{1}{2\Delta\bar{\alpha}^3}\left(\frac{\mathrm{d}\hat{s}(\bar{\alpha}^3)}{\mathrm{d}\bar{\alpha}^3}\right)^{-1}\left(\frac{w^*(\Delta\bar{\alpha}^1, 0, \bar{\alpha}^3 + \Delta\bar{\alpha}^3) + w^*(-\Delta\bar{\alpha}^1, 0, \bar{\alpha}^3 + \Delta\bar{\alpha}^3)}{2}\right. \\ & \left. - \frac{w^*(\Delta\bar{\alpha}^1, 0, \bar{\alpha}^3 - \Delta\bar{\alpha}^3) + w^*(-\Delta\bar{\alpha}^1, 0, \bar{\alpha}^3 - \Delta\bar{\alpha}^3)}{2}\right) \\ & + \delta\cos\omega\left(\frac{u^*(\Delta\bar{\alpha}^1, 0, \bar{\alpha}^3) + u^*(-\Delta\bar{\alpha}^1, 0, \bar{\alpha}^3)}{2}\right) - \delta\sin\omega\left(\frac{v^*(0, \Delta\bar{\alpha}^2, \bar{\alpha}^3) + v^*(0, -\Delta\bar{\alpha}^2, \bar{\alpha}^3)}{2}\right),\end{aligned} \tag{54}$$

where $\Delta\bar{\alpha}^1$, $\Delta\bar{\alpha}^2$ and $\Delta\bar{\alpha}^3$ are constants which will be defined later in this section. The relationship between $\bar{\alpha}^i$ and $(\bar{r}, \phi, \bar{s})$ can be displayed as

$$\bar{\alpha}^1 = \bar{r}\cos(\phi - \omega), \qquad \bar{\alpha}^2 = \bar{r}\sin(\phi - \omega), \qquad \bar{\alpha}^3 = \bar{s} \tag{55}$$

and the relationship between (u^*, v^*, w^*) and (u, v, w) is

$$u^* = u\cos(\phi - \omega) - v\sin(\phi - \omega), \qquad v^* = u\sin(\phi - \omega) + v\cos(\phi - \omega), \qquad w^* = w. \tag{56}$$

With the motivation that the locations at which u and w are evaluated coincide with locations where $u_{[i,j,k]}$ and $w_{[i,j,k]}$ are defined on the staggered grid system respectively, we now choose

$$\Delta\bar{\alpha}^1 = \Delta\bar{\alpha}^2 = \frac{\Delta\bar{r}}{2}, \qquad \Delta\bar{\alpha}^3 = \frac{\Delta\bar{s}}{2}, \qquad \omega = \frac{\Delta\phi}{2}. \tag{57}$$

Using (55)–(57), we rewrite the finite difference approximation (54) in terms of the discrete functions $u_{[i,j,k]}$ and $w_{[i,j,k]}$, namely

$$\begin{aligned}0 = {} & \frac{1}{\eta 1_k \Delta\bar{r}}(u_{[1,1,k]} + u_{[1,M,k]} + u_{[1,M/2+1,k]} + u_{[1,M/2,k]}) \\ & + \frac{1}{8\Delta\bar{s}}(w_{[1,1,k]} + w_{[1,M,k]} - w_{[1,1,k-1]} - w_{[1,M,k-1]}) \\ & - \frac{\delta\sin\phi 1_1}{2}(u_{[1,M/2+1,k]} - u_{[1,M/2,k]}) + \frac{\delta\cos\phi 1_1}{2}(u_{[1,1,k]} - u_{[1,M,k]}),\end{aligned} \tag{58}$$

where we have made use of (20) and evaluated the result at $\bar{s}$ equal to $s1_k$. The discrete equation (58) is a well-defined second-order finite difference approximation to the incompressibility condition (1) for p grid points corresponding to points on the centreline of the pipe.

APPENDIX II

In this appendix we obtain a valid second-order finite difference approximation for $\partial v/\partial\bar{r}$ at grid points adjacent to the centreline, namely for points corresponding to $\bar{r}=r1_1$. This discrete approximation will be used to replace the discrete operator $D_{2r}(v_{[1,j,k]})$ in equations (37)–(40). In a similar manner, second-order finite difference approximations can be obtained for $\partial u/\partial\bar{r}$, $\partial w/\partial\bar{r}$, $\partial^2 u/\partial\bar{r}^2$, $\partial^2 v/\partial\bar{r}^2$, $\partial^2 w/\partial\bar{r}^2$, $\partial^2 u/\partial\bar{r}\partial\bar{s}$, $\partial^2 v/\partial\bar{r}\partial\bar{s}$ and $\partial^2 w/\partial\bar{r}\partial\bar{s}$ for points adjacent to the centreline.

Using the relationship between co-ordinates $\bar{\alpha}^i$ and $(\bar{r}, \phi, \bar{s})$ in equation (55), we obtain

$$\frac{\partial v^*}{\partial\bar{r}} = \frac{\partial v^*}{\partial\bar{\alpha}^1}\frac{d\bar{\alpha}^1}{d\bar{r}} + \frac{\partial v^*}{\partial\bar{\alpha}^2}\frac{d\bar{\alpha}^2}{d\bar{r}} = \frac{\partial v^*}{\partial\bar{\alpha}^1}\cos(\phi-\omega) + \frac{\partial v^*}{\partial\bar{\alpha}^2}\sin(\phi-\omega). \tag{59}$$

Another representation of $\partial v^*/\partial\bar{r}$ can be obtained using (56), as

$$\frac{\partial v^*}{\partial\bar{r}} = \frac{\partial[v\sin(\phi-\omega)]}{\partial\bar{r}} + \frac{\partial[v\cos(\phi-\omega)]}{\partial\bar{r}} = \frac{\partial v}{\partial\bar{r}}\sin(\phi-\omega) + \frac{\partial v}{\partial\bar{r}}\cos(\phi-\omega). \tag{60}$$

Combining the results (59) and (60) for ϕ equal to ω, we obtain

$$\frac{\partial v^*}{\partial\bar{\alpha}^1}(\bar{r}, 0, \bar{s}) = \frac{\partial v}{\partial\bar{r}}(\bar{r}, \omega, \bar{s}) \quad \text{for all} \quad \bar{r} > 0, \tag{61}$$

where use has also been made of (55) evaluated for ϕ equal to ω, namely

$$\bar{\alpha}^1 = \bar{r}, \quad \bar{\alpha}^2 = 0 \quad \text{and} \quad \bar{\alpha}^3 = \bar{s} \quad \text{for} \quad \phi = \omega. \tag{62}$$

Since the co-ordinates $\bar{\alpha}^i$ are non-singular and u^*, v^* and w^* satisfy all the conditions for the applicability of Taylor's theorem, a second-order discrete approximation to $\partial v^*/\partial\bar{\alpha}^1$ at points $(\bar{\alpha}^1, \bar{\alpha}^2, \bar{\alpha}^3) = (r1_1, 0, \bar{s})$ is

$$\frac{\partial v^*}{\partial\bar{\alpha}^1}(r1_1, 0, \bar{s}) = \frac{v^*(3\Delta\bar{r}/2, 0, \bar{s}) - v^*(-\Delta\bar{r}/2, 0, \bar{s})}{2\Delta\bar{r}} + O(\Delta\bar{r})^2, \tag{63}$$

where it should be recalled from (30) that $r1_1 = \Delta\bar{r}/2$. Making use of (20), (55) and (56), it follows from (63) that

$$\begin{aligned}\frac{\partial v^*}{\partial\bar{\alpha}^1}(r1_1, 0, \bar{s}) &= \frac{v(3\Delta\bar{r}/2, \omega, \bar{s}) + v(\Delta\bar{r}/2, \pi+\omega, \bar{s})}{2\Delta\bar{r}} + O(\Delta\bar{r})^2\\ &= \frac{v(3\Delta\bar{r}/2, \omega, \bar{s}) - v(\Delta\bar{r}/2, \pi-\omega, \bar{s})}{2\Delta\bar{r}} + O(\Delta\bar{r})^2.\end{aligned} \tag{64}$$

After combining the results (61) and (64), utilizing the definition of the discrete function $v_{[i,j,k]}$ of Section 3 and evaluating these results for $\omega = \phi 2_j$ and $\bar{s} = s1_k$, we obtain

$$\frac{\partial v}{\partial\bar{r}}(r1_1, \phi 2_j, s1_k) = \frac{v_{[2,j,k]} - v_{[1,M-j,k]}}{2\Delta\bar{r}} + O(\Delta\bar{r})^2, \tag{65}$$

where (65) is a second-order finite difference approximation to $\partial v/\partial\bar{r}$ at v grid points corresponding to $r1_1 = \Delta\bar{r}/2$.

REFERENCES

1. W. R. Dean, 'Note on the motion of fluid in a curved pipe', *Philos. Mag.*, **4**, 208–223 (1927).
2. W. R. Dean, 'The stream-line motion of fluid in a curved pipe', *Philos. Mag.*, **5**, 673–695 (1928).
3. A. E. Green, P. M. Naghdi and M. J. Stallard, 'A direct theory of viscous fluid flow in pipes. II. Flow of incompressible viscous fluids in curved pipes', *Philos. Trans. R. Soc. Lond. A*, **342**, 543–572 (1993).
4. A. E. Green and P. M. Naghdi, 'A direct theory of viscous fluid flow in pipes. I. Basic general developments', *Philos. Trans. R. Soc. Lond. A*, **342**, 525–542 (1993).
5. Z. H. Yang and H. B. Keller, 'Multiple laminar flows through curved pipes', *Appl. Numer. Math.*, **2**, 257–271 (1986).
6. W. Y. Soh and S. A. Berger, 'Fully developed flow in a curved pipe of arbitrary curvature ratio', *Int. j. numer. methods fluids*, **7**, 733–755 (1987).
7. T. J. Pedley, *The Fluid Mechanics of Large Blood Vessels*, Cambridge University Press, New York, 1980.
8. A. J. Ward-Smith, *Internal Fluid Flow*, Clarendon, Oxford, 1980.
9. S. A. Berger, L. Talbot and L.-S. Yao, 'Flow in curved pipes', *Ann. Rev. Fluid Mech.*, **15**, 461–512 (1983).
10. H. Itō, 'Flow in curved pipes', *JSME Int. J.*, **30**, 543–552 (1987).
11. T. Asakura and T. Karino, 'Flow patterns and spatial distribution of atherosclerotic lesions in human coronary arteries', *Circ. Res.*, **66**, 1045–1066 (1990).
12. S. F. C. Stewart and D. J. Lyman, 'Effects of a vascular graft/natural artery compliance mismatch on pulsatile flow', *J. Biomech.*, **25**, 297–310 (1992).
13. S. C. R. Dennis, 'Calculation of the steady flow through a curved tube using a new finite-difference method', *J. Fluid Mech.*, **99**, 449–467 (1980).
14. P. Daskopoulos and A. M. Lenhoff, 'Flow in curved ducts: bifurcation structure for stationary ducts', *J. Fluid Mech.*, **203**, 125–148 (1989).
15. W. Y. Soh and S. A. Berger, 'Laminar entrance flow in a curved pipe', *J. Fluid Mech.*, **148**, 109–135 (1984).
16. A. M. Robertson, 'On viscous flow in curved pipes of variable cross-section', *Ph.D. Thesis*, University of California at Berkeley, 1992.
17. H. B. Keller, *Lectures on Numerical Methods in Bifurcation Problems*, Springer, New York, 1987.
18. I. S. Duff, A. M. Erisman and J. K. Reid, *Direct Methods for Sparse Matrices*, Clarendon, Oxford, 1990.